CELLULAR NEUROSCIENCE

CLIP-Seq analysis enables the design of protective ribosomal RNA bait oligonucleotides against *C9ORF72* ALS/FTD poly-GR pathophysiology

Juan A. Ortega[1,2]†, Ivan R. Sasselli[3,4,5,6]†, Marco Boccitto[7]†, Andrew C. Fleming[1]†, Tyler R. Fortuna[8], Yichen Li[9], Kohei Sato[3,4], Tristan D. Clemons[3,4], Elizabeth D. Mckenna[1], Thao P. Nguyen[1], Eric N. Anderson[8], Jesus Asin[10], Justin K. Ichida[9], Udai B. Pandey[8], Sandra L. Wolin[7], Samuel I. Stupp[3,4,11,12,13], Evangelos Kiskinis[1,4,14]*

Amyotrophic lateral sclerosis and frontotemporal dementia patients with a hexanucleotide repeat expansion in *C9ORF72* (C9-HRE) accumulate poly-GR and poly-PR aggregates. The pathogenicity of these arginine-rich dipeptide repeats (R-DPRs) is thought to be driven by their propensity to bind low-complexity domains of multivalent proteins. However, the ability of R-DPRs to bind native RNA and the significance of this interaction remain unclear. Here, we used computational and experimental approaches to characterize the physicochemical properties of R-DPRs and their interaction with RNA. We find that poly-GR predominantly binds ribosomal RNA (rRNA) in cells and exhibits an interaction that is predicted to be energetically stronger than that for associated ribosomal proteins. Critically, modified rRNA "bait" oligonucleotides restore poly-GR–associated ribosomal deficits and ameliorate poly-GR toxicity in patient neurons and *Drosophila* models. Our work strengthens the hypothesis that ribosomal function is impaired by R-DPRs, highlights a role for direct rRNA binding in mediating ribosomal dysfunction, and presents a strategy for protecting against C9-HRE pathophysiological mechanisms.

INTRODUCTION

Amyotrophic lateral sclerosis (ALS) and frontotemporal dementia (FTD) are two progressive and untreatable neurodegenerative diseases with overlapping genetic abnormalities but divergent clinical presentations. The major genetic cause of both diseases is a heterozygous intronic hexanucleotide $(GGGGCC)_n$ repeat expansion in the *C9ORF72* gene (C9-HRE) (*1*, *2*). C9-HRE causes a reduction in C9ORF72 protein and produces neurotoxic RNA (*3*). Both the sense and antisense GGGGCC expansion can be transcribed and translated into five distinct dipeptide repeat (DPR) proteins [glycine-proline (GP), glycine-alanine (GA), glycine-arginine (GR), proline-arginine (PR), and proline-alanine (PA)] (*4*–*6*). Although the relative pathogenic contribution of these mechanisms to the disease remains unclear, multiple studies have demonstrated that C9-DPRs, and especially the arginine-rich GR and PR, are particularly toxic [reviewed by (*7*–*9*)]. Expression of GR and PR results in cellular toxicity in vitro, as well as stark neurodegeneration in *Drosophila* models, and neurodegeneration and behavioral phenotypes in mouse models in vivo (*10*–*18*).

The pathogenicity of poly-GR and poly-PR is thought to be primarily driven by the propensity of their arginine-rich core sequence to bind to low-complexity domains (LCDs) of multivalent proteins by ionic and cation-pi contacts. A number of mass spectrometry (MS)–based interaction assays have demonstrated that R-DPRs heterogeneously bind to LCD-containing proteins that are associated with multiple cellular functions including RNA metabolism and nucleocytoplasmic (N/C) trafficking (*11*, *15*, *19*–*27*). However, while R-DPRs have been shown to bind RNA in vitro (*11*, *21*, *24*, *26*, *28*), nothing is known about their native interactions with RNA in living cells and the functional consequences of these interactions. To address this critical gap in knowledge, we combined empirical and bioinformatic tools to decipher how the polar nature and the differential secondary structure of R-DPRs determine their interaction with RNA. Cross-linking immunoprecipitation followed by high-throughput sequencing, supported by targeted Northern blot (NB) and quantitative polymerase chain reaction (qPCR) experiments, identified various ribosomal RNA (rRNA) species as direct targets of poly-GR in living cells. This interaction, which occurs in both the nucleus and cytoplasm, disrupts ribosomal homeostasis. On the basis of these findings, we designed a modified rRNA oligonucleotide that acted as a "bait" and inhibited poly-GR–associated ribosomal defects. The rRNA bait ameliorated the toxicity of poly-GR in induced pluripotent stem cell (iPSC)–derived motor neurons and cellular models in vitro and *Drosophila* models in vivo. Our work strengthens the hypothesis that ribosomal function is severely impaired by R-DPRs and suggests that a

[1]The Ken & Ruth Davee Department of Neurology, Feinberg School of Medicine, Northwestern University, Chicago, IL 60611, USA. [2]Department of Pathology and Experimental Therapy, Institute of Neurosciences, University of Barcelona, Barcelona 08907, Spain. [3]Department of Chemistry, Northwestern University, Evanston, IL 60208, USA. [4]Simpson Querrey Institute for BioNanotechnology, Northwestern University, Chicago, IL 60611, USA. [5]Center for Cooperative Research in Biomaterials (CIC biomaGUNE), Basque Research and Technology Alliance (BRTA), Donostia-San Sebastián 20014, Spain. [6]Centro de Fisica de Materiales (CFM), CSIC-UPV/EHU, 20018 San Sebastián, Spain. [7]RNA Biology Laboratory, Center for Cancer Research, National Cancer Institute, Frederick, MD 21702, USA. [8]Department of Pediatrics, Children's Hospital of Pittsburgh, University of Pittsburgh School of Medicine, Pittsburgh, PA 15224, USA. [9]Department of Stem Cell Biology and Regenerative Medicine, Keck School of Medicine, University of Southern California, Los Angeles, CA 90033, USA. [10]Department of Statistical Methods, School of Engineering, University of Zaragoza, Zaragoza 50018, Spain. [11]Department of Biomedical Engineering, Northwestern University, Evanston, IL 60208, USA. [12]Department of Materials Science and Engineering, Northwestern University, Evanston, IL 60208, USA. [13]Department of Medicine, Northwestern University, Chicago, IL 60611, USA. [14]Department of Neuroscience, Northwestern University Feinberg School of Medicine, Chicago, IL 60611, USA.
*Corresponding author. Email: evangelos.kiskinis@northwestern.edu
†These authors contributed equally to this work.

sequence-specific rRNA molecule can abrogate the toxic effects of poly-GR.

RESULTS

C9 arginine (R)-DPRs exhibit differential physicochemical features

To interrogate the role of RNA in DPR pathophysiology, we first characterized the structural and chemical features of R-DPRs. We specifically examined the secondary structure of the R-rich, highly toxic poly-GR and poly-PR by all-atom molecular dynamics (MD) simulations using the CHARMM force field (Fig. 1, A and B). As a control, we looked at the nontoxic poly-GP DPR. We modeled DPRs with 15 repeats, which represents the maximum length of peptides we could synthesize with high purity and corresponds to half of the minimum number of hexanucleotide $(GGGGCC)_n$ repeats that is considered to be neurotoxic (n = 30). While both $(GP)_{15}$ and $(GR)_{15}$ showed a highly coiled conformation, $(PR)_{15}$ displayed a more stretched structure (Fig. 1, A and B, and fig. S1A). The differential physicochemical properties of proline and glycine likely affect the differential conformation of DPRs, with proline favoring a rigid backbone and glycine conferring higher flexibility (*29*). Along these lines, the calculation of torsional angles in the different DPR residues by Ramachandran plots showed that $(PR)_{15}$ has a high enrichment in β sheet conformations, while $(GR)_{15}$, and $(GP)_{15}$ displayed a more diverse profile of different secondary conformations in their structures (Fig. 1C). This correlates with a higher extended conformation observed in $(PR)_{15}$, while $(GP)_{15}$ and $(GR)_{15}$ show more convoluted structures (Fig. 1B). To validate the results obtained by MD simulations, we synthesized highly pure DPRs with 15 repeats (fig. S1B) and characterized them by circular dichroism (CD) (*30*). Using spectra of proteins and peptides with highly pure secondary structure contributions as a reference, we obtained qualitative information of the major secondary structures in C9-DPRs (Fig. 1, D and E). We found that while $(PR)_{15}$ showed a β sheet spectrum with the characteristic negative peak over 210 nm, $(GP)_{15}$ showed two negative peaks, typical of an α helix, and $(GR)_{15}$ displayed a random-coiled spectrum (Fig. 1D). Additionally, we used the BeStSel tool (*31*) to analyze the secondary structure ratios in the three distinct DPR proteins, and found major contributions of helix, sheet, and coil conformations in $(GP)_{15}$, $(PR)_{15}$, and $(GR)_{15}$, respectively (Fig. 1F).

Given the unique nature of R-DPRs and the lack of any similar datasets for comparison, we used additional techniques to confirm our results. We specifically performed liquid and solid sampling of the C9 DPRs and used Fourier transform infrared spectroscopy (FTIR), which allows for collecting high-resolution spectral data without a potential impact of solvent composition. We focused on the amide I region, as this vibrational mode is known to be highly sensitive to peptide secondary structure and the shift of the signals is benchmarked for the different types of secondary structures (*32*). FTIR is not affected by the loss of chirality in glycine-rich sequences, but it can present overlapping signals and interference from other chemical groups, and thus, signal deconvolution is essential. We observed contributions from the arginine's side chain (Arg I and Arg II) at 1587 and 1608 cm^{-1} for $(GR)_{15}$ (Fig. 1G) (*32*), while for $(PR)_{15}$ the latter peak [red arrow in $(GR)_{15}$ signal] is merged with the β sheet contribution of amide I, giving a peak at around 1615 cm^{-1} (blue arrow). In contrast, the main amide I contribution of $(GR)_{15}$ is displayed at 1648 cm^{-1}, typical of random coil (Fig. 1G) (*32*, *33*). $(GP)_{15}$ displayed a sum of amide I vibrations with similar intensity, suggesting that it exhibits a combination of β sheet, random coil, α helix, and turn conformations. The deconvolution shows the strong relevance on the random coil mode to the final spectra and highlights the α-helix contribution in the three peptides, which is typically masked by other peaks. This contribution is especially important in $(GP)_{15}$. While all three DPRs exhibited a signal at 1675 cm^{-1}, typical of rigid turns, this was strongly enhanced in R-DPRs (Fig. 1G), likely reflecting the additional intramolecular R-R interactions that R-DPRs form as shown in the MD simulations. In solid FTIR analysis, the arginine side-chain vibrations disappear, validating the β sheet nature of the $(PR)_{15}$ amide I vibration around 1620 cm^{-1} (fig. S1C). In contrast, $(GP)_{15}$ and $(GR)_{15}$ exhibited higher amide I frequencies, indicative of a random-coiled structure that is more predominant for $(GR)_{15}$ (fig. S1C).

We next asked how the number of repeats would affect the structure of the DPRs using MD simulations. Ramachandran plots of both GR and PR with 10, 20, 30, and 50 repeats showed the same secondary structure patterns, irrespective of length (Fig. 1H and fig. S1D). The higher flexibility of the poly-GR backbone favors a more folded conformation compared to the poly-PR backbone, which exhibited an extended conformation (Fig. 1H and fig. S1E). Accordingly, the higher level of folding observed in poly-GR peptides led to a size-dependent increase in the number of R-R and H-bond interactions within the peptide backbone relative to poly-PR (Fig. 1, I and J, and fig. S1F). We also performed MD simulations to interrogate the intrinsic aggregation propensity (AP) of different size R-DPRs. As a positive control, we used poly-GA because of its well-described tendency to self-aggregate (fig. S1, G to J) (*7*, *29*, *34*). Although R-DPRs displayed reduced AP profiles compared to poly-GA, the AP values in poly-PR were slightly higher than those in poly-GR (fig. S1K). Collectively, our computational and empirical analyses indicate that GR and PR exhibit differential secondary structures and APs that appear to be only mildly affected by repeat length and could lead to differential pathophysiological effects.

C9 R-DPRs interact with RNA in vitro

Previous studies have suggested that R-DPRs can bind to RNA molecules through ionic and cation-pi interactions and undergo liquid-liquid phase separation (*21*, *24*, *28*). Thus, we sought to assess whether the differential physicochemical properties of poly-GR and poly-PR DPRs would affect their binding to RNA molecules. We first incubated total human RNA with synthetic DPRs in vitro and measured optical density as an indicator of RNA-DPR interaction (Fig. 2A and fig. S2A). While $(GP)_{15}$ had no effect, both R-DPRs form complexes with RNA in a concentration-dependent manner (Fig. 2A). A dose-response experiment with increasing concentrations of DPRs showed that the interaction of $(GR)_{15}$ with RNA peaked at 20 μM, while $(PR)_{15}$ peaked at 15 μM, suggesting a stronger potential for PR to bind to RNA (Fig. 2A). This is in accordance with its expanded structural conformation (Fig. 1 and fig. S1) and, by extension, the higher number of cations available for multiple electrostatic or cation-pi interactions with RNAs (Fig. 2B). Calculation of the solvent-accessible surface area (SASA) of both R-DPRs and poly-GP indicated higher values in poly-(PR) than the other DPRs, particularly for the 15 and 30

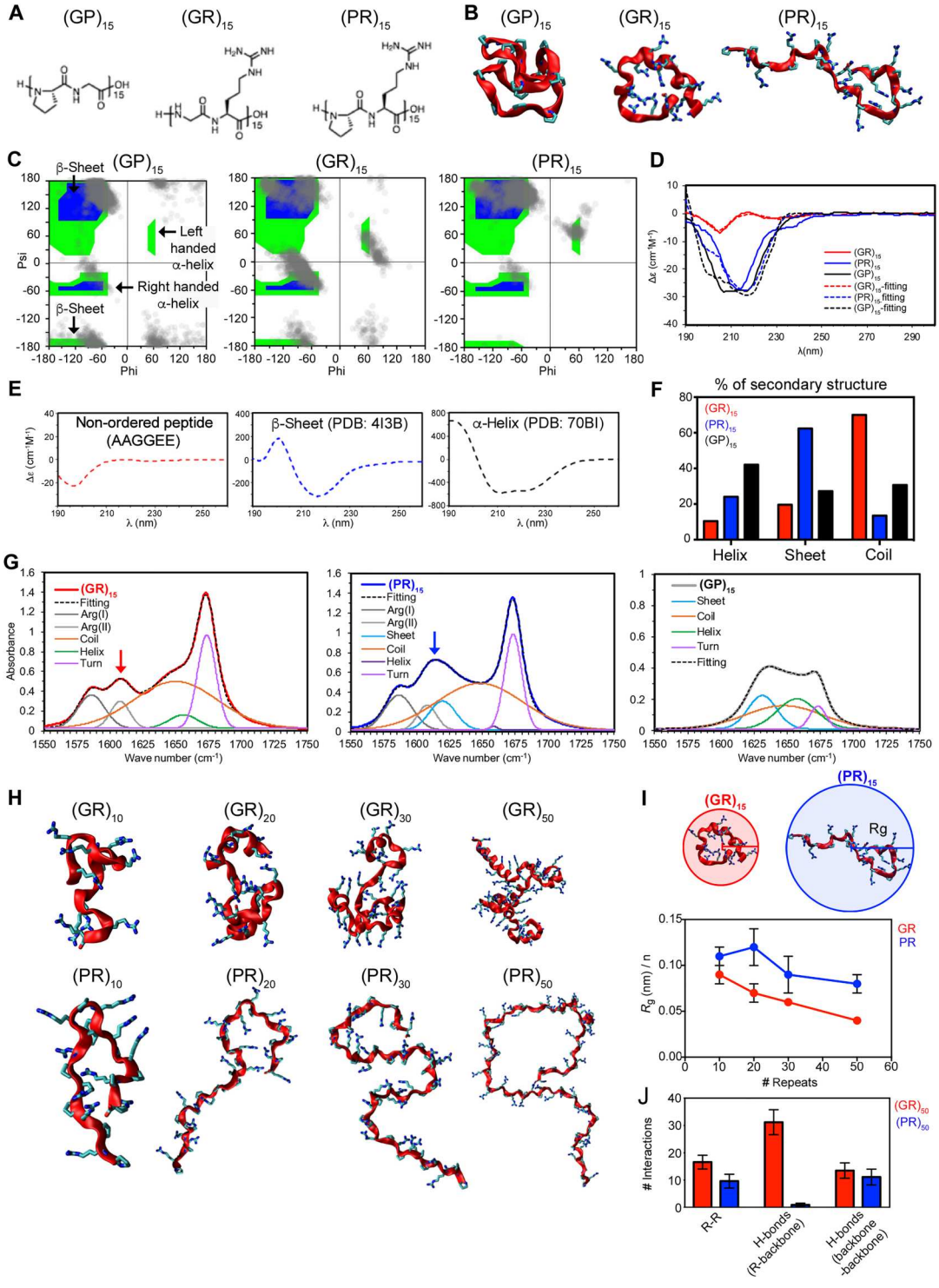

Fig. 1. Computational and empirical characterization of the physicochemical features of C9 R-DPRs. (**A**) Chemical structures of $(GP)_{15}$, $(GR)_{15}$, and $(PR)_{15}$. (**B**) $(GP)_{15}$, $(GR)_{15}$, and $(PR)_{15}$ structures after all-atom MD simulations. Backbone displays secondary structure; side-chain hydrogens are omitted for clarity. (**C**) Ramachandran plots mapping the frequencies of secondary structures (gray dots) within $(GP)_{15}$, $(GR)_{15}$, and $(PR)_{15}$. Green and blue areas identify different types of dihedral angles associated to β sheets, left- and right-handed α helices. (**D**) Line graphs showing the secondary structure traces of 1 mM $(GP)_{15}$, $(GR)_{15}$, and $(PR)_{15}$ in 10 mM Hepes, 10 mM NaCl (pH 7.2), analyzed by circular dichroism (CD). Dashed lines denote the fitting convolution of CD spectra. (**E**) Line graphs showing the CD traces of reference peptides: nonordered, β sheet rich (PDB: 4I3B), and α-helix rich (PDB: 7OBI). (**F**) Bar plot showing the percentage of secondary structures in $(GP)_{15}$, $(GR)_{15}$, and $(PR)_{15}$ based on CD analysis. (**G**) Line graph showing FTIR spectra of $(GP)_{15}$, $(GR)_{15}$, and $(PR)_{15}$ in the amide I region. Spectra were deconvoluted to show the secondary structure traces (sheet, coil, helix, and turn) and arginine side-chain contributions (Arg I and Arg II). Hepes solution was used as a control. (**H**) All-atom MD simulations of secondary structures of $(GR)_n$ and $(PR)_n$ with different repeat numbers. (**I**) Top: Schematic representation of $(GR)_{15}$ and $(PR)_{15}$ peptide length calculation measured by the radius of the circle that circumscribes each R-DPR. Bottom: Bar graph depicting the radius of gyration (R_g) measured in the simulations of R-DPRs with different repeat numbers. Values represent mean ± standard deviation (SD). (**J**) Bar plot showing the number of R-R and H-bond (within the backbone or between backbone and R residues) interactions in R-DPRs. Values represent mean ± SD.

repeat dipeptides (Fig. 2C and fig. S2B). We next interrogated how the concentration of RNA would affect the propensity for R-DPRs to phase separate. We observed that while the gradual increase in RNA concentration of up to 10 μg/μl increased the optical density values, higher concentrations reduced phase separation (Fig. 2D), suggesting that the interaction is both RNA and R-DPR concentration dependent. Finally, we asked whether the R-DPRs differentially interact with distinct types of RNA, including ribosomal (rRNA), transfer (tRNA), and messenger RNA (mRNA) in vitro. We found that both R-DPRs interacted more strongly with rRNA than mRNA (Fig. 2E), correlating with the fact that in cells they accumulate in nucleoli (fig. S2, C and D). Moreover, $(GR)_{15}$

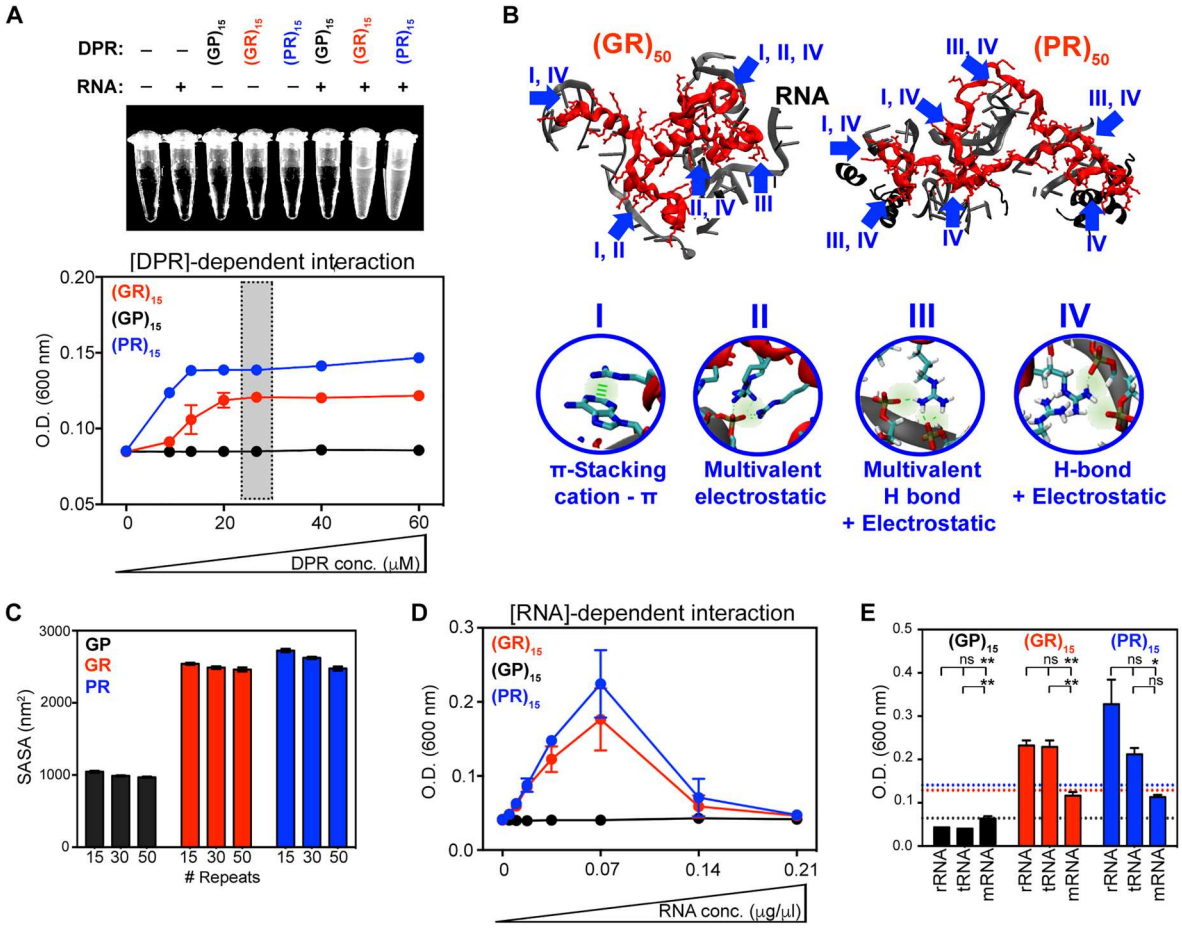

Fig. 2. Characterization of the interaction between R-DPRs and RNA in vitro. (**A**) Top: Photograph of turbidity assays after mixing human total RNA and synthetic $(GP)_{15}$, $(GR)_{15}$, and $(PR)_{15}$. Bottom: Line graph depicting DPR concentration-dependent precipitation of 0.07 μg/μl RNA calculated by optical density (O.D.). Gray shaded area indicates the DPR concentration used in (D). (**B**) MD simulation snapshots showing how differential secondary structures in R-DPRs (red) can influence the number and type of interactions with human ribosomal RNA (rRNA; gray/black). Bottom: Circles showing the different types of interactions that could mediate the binding of $(GR)_{50}$ and $(PR)_{50}$ with rRNA. (**C**) Bar graph indicating the solvent-accessible solvent area (SASA) measured from MD simulations of $(GP)_n$, $(GR)_n$, and $(PR)_n$ with different number of repeats (n = 15, 30, and 50). (**D**) Line graph depicting RNA concentration–dependent precipitation of $(GR)_{15}$, $(GP)_{15}$, and $(PR)_{15}$ calculated by optical density measurements. (**E**) Bar graph showing turbidity assay measurements used to assess the level of interaction of 26.7 μM $(GP)_{15}$, $(GR)_{15}$, and $(PR)_{15}$ with 5 μg/μl ribosomal (rRNA), transfer (tRNA), and messenger (mRNA) RNA. Dot lines indicate the level of interaction of the distinct DPRs with total human RNA. All values are presented as the mean ± SD. ANOVA: $^*P < 0.05$; $^{**}P < 0.01$; ns, not significant.

exhibited a stronger interaction with tRNA than mRNA (Fig. 2F). Collectively, our findings are in line with previous studies in demonstrating that poly-R-DPRs bind RNA molecules in vitro (*21*, *28*), and suggest that R-DPRs may have differential preferences for binding to distinct types of RNAs.

Poly-GR binds to rRNA in cells

We next sought to identify the RNAs bound by poly-GR in live cells. We focused our analysis on poly-GR since GR-positive aggregates are more frequently observed in C9-ALS/FTD patient tissue relative to PR aggregates (*4*, *35*, *36*), and its abundance has been associated with affected brain areas in patients (*37*). We used cross-linking immunoprecipitation (IP) followed by high-throughput sequencing (CLIP-Seq) (*38*) to identify targets of poly-GR on a transcriptome-wide scale. In CLIP-Seq, ultraviolet (UV) light is used to cross-link proteins to RNAs that are in direct contact in live cells. After immunoprecipitating the protein of interest and harsh washing to remove noncovalently associated RNA, complementary DNA (cDNA) is prepared from the cross-linked RNA and sequenced (Fig. 3A). In preliminary experiments, we confirmed that, following transfection into human embryonic kidney (HEK)–293 cells, GFP-$(GR)_{50}$ could be crosslinked to RNA (fig. S3, A to C). To identify specific targets, we transfected HEK-293 cells with GFP-$(GR)_{50}$, using GFP (green fluorescent protein) (Fig. 3B) or GFP-$(GP)_{10}$ and untransfected cells (fig. S3D) as controls. Following UV-crosslinking, IP, and cDNA sequencing, we found that GFP-$(GR)_{50}$ interacted predominantly with rRNA. In two biological replicates, 96% and 92% of the GFP-$(GR)_{50}$ CLIP peaks, defined as five or more overlapping sequencing reads at a specific genomic locus, mapped to ribosomal DNA (rDNA) (Fig. 3C, fig. S3E, and table S2). Additionally, while 63% and 68% of the CLIP peaks from the control samples also mapped to rDNA, the rRNA-derived peaks were strongly enriched in GFP-$(GR)_{50}$ immunoprecipitates, while tRNAs and Y RNAs that are also highly

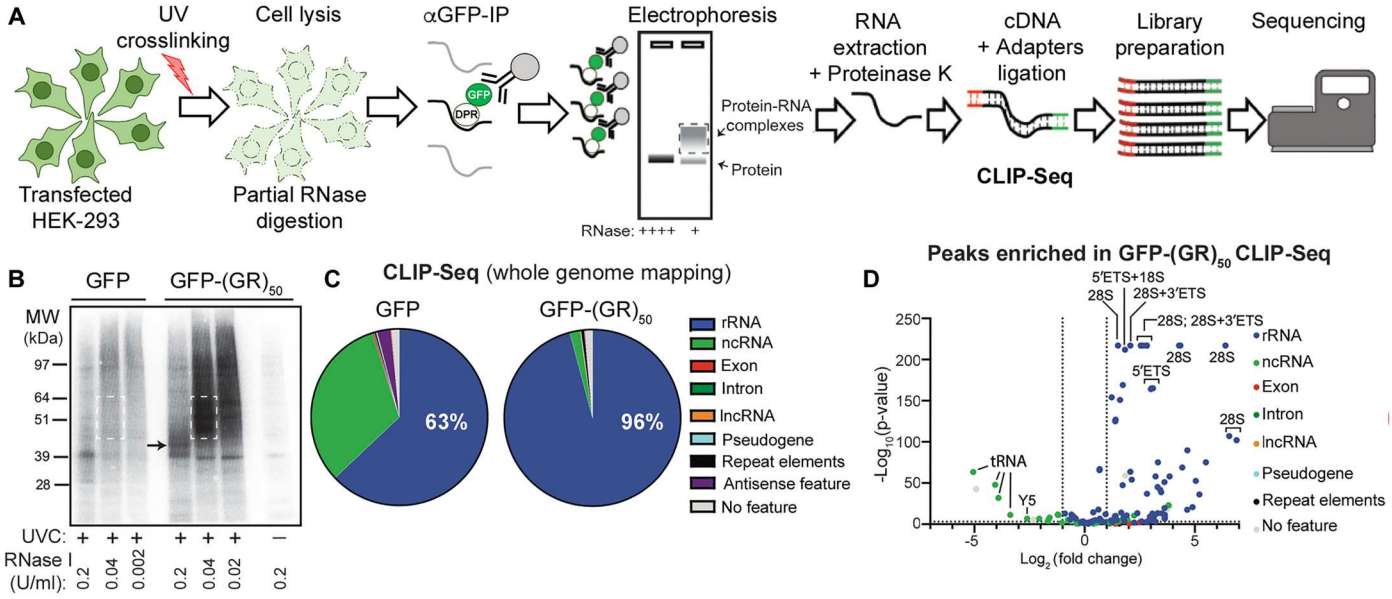

Fig. 3. Characterization of the interactions between poly-GR and RNA in live cells. (**A**) Experimental schematic. (**B**) Partial ribonuclease (RNase) digestion to generate clonable fragments and IP with anti-GFP antibodies. Ribonucleoproteins (RNPs) in immunoprecipitates were labeled at the 5′ end with [γ-^{32}P]ATP and fractionated using SDS-PAGE. After transfer to a membrane, RNPs were detected with autoradiography. White dashed lines: RNPs excised for library preparation. Arrow: GFP-$(GR)_{50}$. (**C**) Pie charts showing the percentage of CLIP-Seq peaks (replicate #1) found in various RNA classes in GFP- versus GFP-$(GR)_{50}$–transfected cells. Peaks defined as having five or more overlapping reads. (**D**) Volcano plot showing CLIP-Seq peaks enriched in GFP-$(GR)_{50}$ compared to GFP in CLIP-Seq (replicate #1). Negative $\log_2$ (fold change) value indicates peaks that were more abundant in the GFP control. Significantly enriched peaks in GFP-$(GR)_{50}$–transfected cells are labeled.

abundant in cells were de-enriched in GFP-$(GR)_{50}$ samples (Fig. 3D and fig. S3F). Close inspection of the RNA45SN1 locus revealed that the GFP-$(GR)_{50}$–derived peaks were not distributed evenly across the rDNA, but rather occurred in specific regions (Fig. 4A and fig. S3G).

Human rDNA exists as hundreds of copies of tandem repeats on five chromosomes (*39*). Although these repeats are not included in the assembled hg38 genome, five complete rDNA sequences that exist outside these clusters are included (RNA45SN1 to RNA45SN5). Additionally, the genome is littered with divergent and truncated rRNA sequences that do not code for bona fide rRNA (*40*). Thus, to simplify quantification of the rRNA-derived reads, we remapped data from the CLIP experiments to a single full-length rDNA sequence, the RNA45SN1 locus [National Center for Biotechnology Information (NCBI) accession no. 146117.1]. We found that 69% and 81% of the total reads aligned to rDNA for the GFP-$(GR)_{50}$ libraries (fig. S3H). In contrast, only 22% of the reads in the GFP control and 23% of the GFP-$(GP)_{10}$ control libraries mapped to rDNA (fig. S3H). The overwhelming majority of GFP-$(GR)_{50}$ reads were derived from the 28S region of the rDNA, with 52% and 63% of the total reads in the two libraries aligning to this region. Within the 28S rRNA, a prominent peak was located between nucleotides 2744 and 2810. This 66-nucleotide (nt) region was the most highly enriched site in both CLIP experiments, accounting for 30% and 45% of total reads in the GFP-$(GR)_{50}$ samples. An additional 57-nt peak at the 3′ end of the 5.8S rRNA accounted for approximately 7% and 9% of the reads in the two GFP-$(GR)_{50}$ datasets. Since mapping to rRNA is often considered nonspecific in CLIP-Seq experiments due to the abundance of rRNA, as an additional control we compared our results with rRNA-derived reads in datasets that were generated using the same iCLIP protocol (*41*). We asked whether iCLIP datasets examining two abundant RNA binding proteins, HNRNPA1 or YTHDC2, contain similar rRNA-derived reads as poly-GR. We did not observe any substantial overlap in the sites of interaction, further suggesting that the binding between rRNA and GFP-$(GR)_{50}$ we identified is highly specific (fig. S3I).

Since the production of mature rRNA involves a complex series of processing steps that occur almost entirely within nuclei, the GFP-$(GR)_{50}$ CLIP peaks that we detected mapping to the 28S and 5.8S sites in the rDNA could be derived from nuclear precursors such as 47S, 45S, 30S, or 32S, and/or the mature cytoplasmic forms (5.8S, 28S) (Fig. 4B). To further characterize the bound rRNAs and distinguish precursors from mature rRNA species, we used ribonucleoprotein immunoprecipitation (RIP) followed by NB analysis. These experiments revealed that mature 28S, 18S, and 5.8S rRNAs were all detected in GFP-$(GR)_{50}$, but not in GFP immunoprecipitates (Fig. 4, C and D). Consistent with specific binding, two other abundant RNAs, the SRP 7SL and the ribonuclease (RNase) P RPPH1 RNA, were not detected in these immunoprecipitates. While these data demonstrate an association between GFP-$(GR)_{50}$ and mature rRNA, some CLIP reads could only have originated from immature rRNA (fig. S3H). The 5′ external transcribed spacer (ETS) and internal transcribed spacer 1 (ITS1) regions were the most abundant precursor regions detected, each accounting for 0.7 to 1.3% of the reads in the GFP-$(GR)_{50}$ CLIP datasets. Because these pre-rRNAs were not abundant enough to detect by NB, we assayed for their presence in our RIP experiment using real-time qPCR (RT-qPCR). Consistent with our NB results, RT-qPCR showed strong enrichment of mature 28S and 18S rRNAs in the GFP-$(GR)_{50}$ immunoprecipitates, as well as for sequences from the 5′ ETS and ITS1 regions of the pre-rRNA (Fig. 4E).

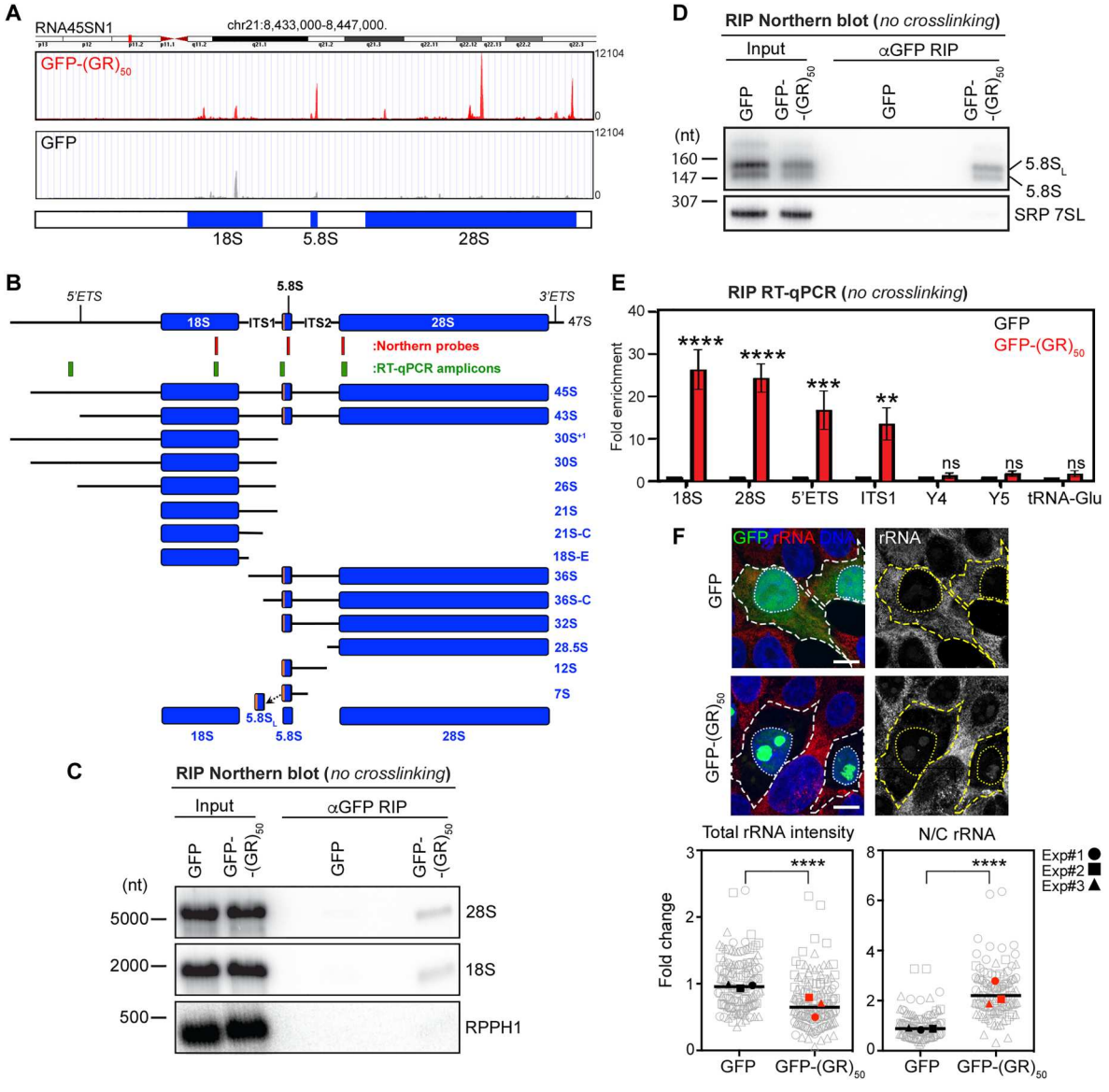

Fig. 4. Poly-GR binds to multiple rRNA species in live cells. (**A**) Distribution of reads mapping to the RNA45SN1 locus from the GFP-$(GR)_{50}$ (top) and GFP (bottom) immunoprecipitates. (**B**) Schematic depicting rRNA processing and precursors detected in human cells (*144*). Probes used for NB and RT-qPCR amplicons are labeled. (**C** and **D**) Lysates of HEK-293 cells expressing GFP-$(GR)_{50}$ or GFP were subjected to IP with anti-GFP antibodies. RNAs within immunoprecipitates were fractionated in denaturing agarose (C) or polyacrylamide (D) gels, and RNAs were detected by NB. Input represents 2% of the lysate used in IP. (**E**) RT-qPCR quantification of RNAs after IP in anti-GFP and anti-GFP-$(GR)_{50}$ immunoprecipitates. Fold enrichment of each RNA relative to the anti-GFP control is shown. $n = 3$ independent biological replicates. Values represent mean ± standard error of the mean (SEM). Two-way ANOVA: $^{**}P < 0.005$; $^{***}P < 0.0002$; $^{****}P < 0.0001$. (**F**) Top: Confocal images of GFP- and GFP-$(GR)_{50}$–transfected cells immunolabeled with an anti-rRNA antibody. Nuclei counterstained with Hoechst 33342. Scale bar, 20 μm. Bottom: Dot plots showing rRNA intensity in whole cells or N/C ratio ($n = 147$, left, and $n = 116$, right, cells per condition). Individual cells from three experiments are represented by distinct shaped symbols in gray, median values of each experiment are represented by distinct shaped symbols in color, and bars represent the global median per condition. Multiple comparisons of means: Tukey contrasts: $^{***}P < 0.001$.

Noncoding Y RNAs and tRNA-Glu were selected as controls since these RNAs were not enriched in the GFP-$(GR)_{50}$ CLIP-Seq dataset (Fig. 3D). As expected, these RNAs showed no significant enrichment in the GFP-$(GR)_{50}$ RIP coupled to RT-qPCR analysis (Fig. 4E).

To validate the selective interaction between rRNAs and $(GR)_{50}$ relative to other C9-DPRs, we performed RIP RT-qPCR analysis in cells transfected with GFP-$(GR)_{50}$ or GFP-$(GA)_{50}$. These experiments revealed that 18S, 28S, and ITS1 rRNAs were again significantly enriched within the GFP-$(GR)_{50}$ immunoprecipitates relative to GFP-$(GA)_{50}$ (fig. S3J).

To further characterize the rRNAs associated with GFP-$(GR)_{50}$, we examined the 3′ ends of the 18S rRNA in GFP-(GR)50 IPs. Although 28S and 5.8S rRNA are entirely matured in the nucleolus, the final step in 18S rRNA maturation occurs in the cytoplasm. Following an endonucleolytic cleavage in the nucleolus that generates

the 18S-E precursor, which contains 78 or 81 extra 3′ nucleotides (Fig. 4B), this precursor is matured by a combination of exonuclease trimming and endonuclease cleavage, with the final 24 nucleotides removed in the cytoplasm (*42*). This cytoplasmic maturation step is one of several mechanisms that prevent premature engagement of the ribosomal machinery with mRNA. Since RIP followed by NB lacks the resolution to distinguish these incompletely processed 18S rRNAs, we carried out 3′ rapid amplification of cDNA ends (RACE) followed by Southern blotting (SB). After performing RIP on GFP-$(GR)_{50}$– and GFP-$(GA)_{50}$–expressing cells, where GFP-GR_{50} is present in both the nucleus (~70%) and cytoplasm (~30%) (fig. S2, C and D), we ligated a 3′ adaptor to the isolated RNA and used real-time PCR to amplify DNA containing the last 108 nucleotides of the mature 18S 3′ end. Precursors containing extended 18S rRNA were detected by probing SBs of the amplified cDNA with an oligonucleotide that preferentially detects the 3′ extended species (fig. S4A). Although cDNAs corresponding to the 3′ extended RNAs were detected in both input RNA samples and the GFP-$(GA)_{50}$ IP, cDNA corresponding to these precursors was undetectable in the GFP-$(GR)_{50}$ IP (fig. S4A). In contrast, probing with an oligonucleotide that detects the mature 18S 3′ end revealed that mature 18S rRNA is highly enriched in the GFP-$(GR)_{50}$ IP compared to the GFP-$(GA)_{50}$ IP (fig. S4B). Thus, although constitutively expressed GFP-$(GR)_{50}$ is abundant in nuclei, most of the 18S rRNA that coprecipitates with GFP-$(GR)_{50}$ is the mature cytoplasmic species.

Last, to determine whether the highly enriched interaction of $(GR)_{50}$ with rRNAs is driven by its subcellular localization to the nucleolus, we used a cellular model where $(GR)_{50}$ was predominantly cytoplasmic. We established an efficient doxycycline-inducible GFP-$(GR)_{50}$ cell line and monitored the subcellular localization of GFP-$(GR)_{50}$. We found that during the first 18 hours after induction of expression, as much as 88% of $(GR)_{50}$ accumulates in the cytoplasm (fig. S4C). This is in stark contrast to the previous model we used to perform the CLIP-Seq where as much as 70% of $(GR)_{50}$ accumulated in the nucleus (fig. S2, C and D). Despite the difference in localization, RIP RT-qPCR analysis again identified very strong enrichment of 28S and 18S rRNA sequences in Tet-GFP-$(GR)_{50}$ relative to Tet-GFP control immunoprecipitates, while as expected the pre-rRNA 5′ ETS and ITS1 sequences that are strictly nucleolar and much less abundant, were not enriched in the GFP-$(GR)_{50}$ IP under these conditions (fig. S4D).

Collectively, these results demonstrate that poly-GR binds to multiple rRNA species, including precursors found in the nucleolus and mature RNAs found in both the nucleolus and within fully assembled cytoplasmic ribosomes (fig. S4E). These interactions could

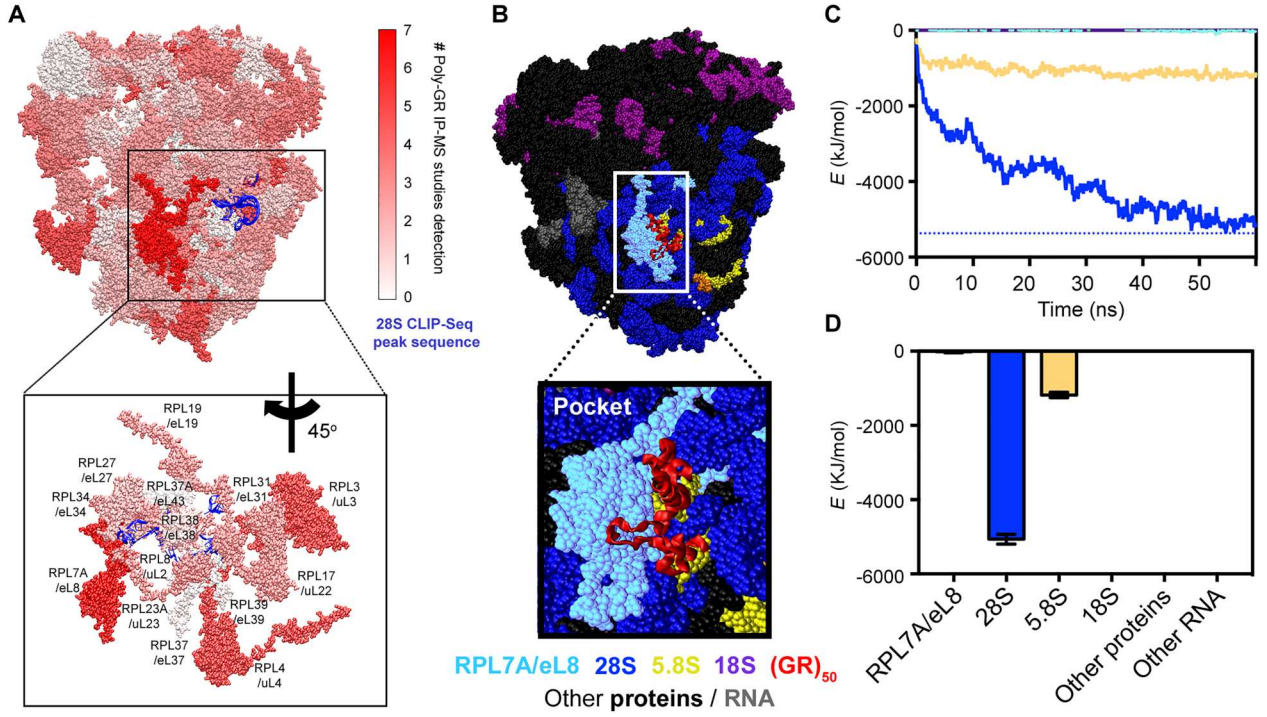

Fig. 5. Computational modeling of poly-GR binding to rRNA and protein subunits. (**A**) Top: Representative image recreated by all-atom MD simulations of all mammalian RPs colored based on the number of studies that identified them as poly-GR interactors. The 28S rRNA sequence identified by our CLIP-Seq analysis is displayed in blue. Bottom: Higher magnification of the mammalian ribosome proteome showing a region around the only protein that was coprecipitated with poly-GR in all seven studies, RPL7A/eL8, which is in close proximity to the 28S rRNA sequence identified by our CLIP-Seq analysis. (**B**) Representative image recreated by all-atom MD simulations of $(GR)_{50}$ interacting with the mammalian ribosome. On the basis of our CLIP-Seq data and previous proteomic data (IP-MS), we determined a poly-GR interaction region ("pocket") magnified in the inset at the bottom. The targeted RPs and RNAs were color-labeled as follows: RPL7A, turquoise; 28S, blue; 5.8S, yellow; 18S, purple. Other proteins and RNAs are labeled in black and gray, respectively. (**C**) Line graph indicating the energetic strength of the interactions of $(GR)_{50}$ in the pocket region of the ribosome over time. $E > 0$ indicates repulsion; $E < 0$ indicates attraction. The energy of interaction for 28S (blue), 5.8S (yellow), 18S (purple), and RPL7A (turquoise) is shown by each line. Dashed line indicates the highest interaction energy achieved between $(GR)_{50}$ and 28S rRNA. (**D**) Bar graph showing average energy of interaction of $(GR)_{50}$ with different ribosomal components as in (C) during the last 10 ns, when structure is considered stable. Values are presented as mean ± SD.

potentially affect ribosomal assembly, homeostasis, and/or function. In line with previous studies (*11*, *24*), immunolabeling to detect rRNA revealed reduced levels of total rRNA in cells transfected with poly-GR (Fig. 4F). We found a significant shift in the N/C ratio of rRNA in cells transfected with GFP-$(GR)_{50}$ (Fig. 4F). We also validated that this shift in rRNA occurs within cortical neurons in postmortem *C9ORF72* ALS/FTD tissue using immunohistochemistry (IHC) (fig. S4, F to H). This increased N/C ratio of rRNA, which suggests impaired ribosomal homeostasis, likely contributes to the previously described reduced level of translation in poly-GR–containing cells (fig. S4I) (*11*, *17*, *19*, *43*).

The interaction of poly-GR with rRNA strongly contributes to ribosomal binding

The identification of rRNA as a binding partner for poly-GR is well aligned with previous MS-based studies in cell models that have consistently uncovered ribosomal proteins (RPs) as GR-DPR interactors after IP (Fig. 5A, fig. S5A, and table S3) (*11*, *15*, *17*, *19*, *23*, *27*, *44*). Similarly, IHC analyses in animal models and postmortem patient tissue have shown strong colocalization between GR and RPs in neurons (*13*, *17*, *19*). In fact, 89% and 94% of all RPs of the small and large ribosomal subunits, respectively, have been reported to precipitate along with poly-GR in at least one of the previously reported interactomes (fig. S5, A and B). One study showed that more than 40% of interactions with RP subunits disappear after RNA degradation by RNase treatment, suggesting that rRNA might be playing a critical role in the physical association of the ribosome with C9 poly-GR DPR (fig. S5C) (*44*). To investigate the significance of the GR-rRNA interaction more directly, we sought to model the poly-GR–ribosome complex. We used cryo–electron microscopy (EM)–based structural information of the mammalian ribosome [Protein Data Bank (PDB) ID: 5LZS] (*45*) and observed that some regions of the 5.8S and 28S rRNA, which were crosslinked to poly-GR in live cells, are exposed to the surface of the fully assembled ribosome (Fig. 5, A and B). One of the closest RPs within this region is RPL7A/eL8, which is the only RP that has been identified in all seven published poly-GR interactome experiments, and one that we validated in our model system (Fig. 5A and fig. S5, A, D, and E) (*11*, *15*, *19*, *23*, *27*, *44*).

On the basis of this converging evidence from proteomic and transcriptomic experiments, we established an in silico model and mapped one of the regions that poly-GR can bind to, on the surface of the ribosome (Fig. 5B and fig. S5, F to I). This potential binding "pocket" within the modeled poly-GR–ribosome assembly accommodates the physicochemical interaction of poly-GR with both rRNA and RPs. To better understand the dynamics of this interaction, we performed MD simulations. We specifically asked how strongly the different ribosomal components that are aligned either within the pocket (RPL7A/eL8, 5.8S, 28S, and 18S) or in close proximity to the pocket (other proteins and RNA) contribute to the binding with $(GR)_{50}$ by comparing their energy of interaction ($E < 0$ attractive and $E > 0$ repulsive) (Fig. 5, B to D, and figs. S5, F to I, and S6, D to G). This analysis showed that the 28S rRNA had the highest energy of interaction with $(GR)_{50}$ ($E = -4004.79$ kJ/mol), followed by 5.8S ($E = -1059.01$ kJ/mol), while RPL7A/eL8 and 18S exhibited negligent E values (Fig. 5, C and D). We also simulated the interaction of $(GR)_{50}$ in a different ribosomal region, where there are RPs that have never been immunoprecipitated with poly-GR (no GR-RP interaction control region) (fig. S6, A to G). We found that $(GR)_{50}$ interacted exclusively with 18S rRNA in this region, although with weaker energy of interaction relative to the one exhibited for 28S rRNA in the pocket region (Fig. 5C and fig. S6H). Of note, $(GR)_{50}$ acquires a more folded configuration within the pocket than within the control region (fig. S6, F and G), suggesting a higher level of conformational adaptation in the pocket, likely due to its stronger interaction with the 28S rRNA. Thus, our computational and CLIP-Seq data (Figs. 3 to 5) suggest that interactions between poly-GR and rRNA contribute to ribosomal binding.

Custom rRNA oligonucleotides bind poly-GR and inhibit the toxic effects of poly-GR in multiple model systems

Collectively, our data indicate that the physicochemical properties of poly-GR promote strong interactions with RNA, while independent transcriptomic and proteomic analysis suggests that GR-DPR can interact with multiple rRNA species and protein subunits (Figs. 3 to 5 and figs. S3 to S6). These interactions can take place with both assembling ribosomal subunits in the nucleus and mature cytoplasmic ribosomes (*17*, *19*), and likely contribute to an impairment in ribosomal homeostasis and function (figs. S4E, S5, and S6). Our dynamic simulation models suggest that the strong rRNA-GR binding may mediate the interaction between the R-DPR and the ribosome. We thus reasoned that an RNA molecule of the right sequence and structure could act as a bait for poly-GR, binding to it and sequestering it away from pathological interactions with other proteins and RNAs.

To test this hypothesis, we used the 28S rRNA sequence that was strongly enriched in our CLIP-Seq experiments and designed an RNA oligonucleotide bait with 2′-*O*-methyl modifications in both the 5′ and 3′ ends to enhance its stability and binding properties (Fig. 6A and Materials and Methods). As a control, we designed a scrambled RNA oligonucleotide of the same length and percentage of nucleotide composition (Fig. 6A). Using dynamic simulations, we observed that both molecules form highly folded structures with similar dimensions and characteristics (Fig. 6A; fig. S7, A to C; and table S5). Specifically, the radius of gyration (R_g) for the 28S and the scrambled rRNA baits was calculated at 1.07 ± 0.01 and 1.09 ± 0.03 nm, respectively (fig. S7C). Notably, the 28S rRNA bait exhibited an almost 50% higher number of base:base hydrogen bonds than the scrambled (14 ± 2 versus 8 ± 1 respectively; fig. S7D), suggesting a higher level of order, and conversely reduced level of dynamism reflected by higher root mean square fluctuation (RMSF) values (fig. S7B). These properties result in a higher exposure of the charged phosphate groups on the exposed surface of the RNA molecule (Fig. 6A). Further, we used MD simulations to model the interaction between DPRs and the RNA baits, and we observed evident differences between $(GR)_{50}$ and the R-free DPRs $(GP)_{50}$ and $(GA)_{50}$ (fig. S7, E to H). While poly-GP and poly-GA maintain their folded structures and show very little interaction with the baits, poly-GR "engulfs" the RNA baits (fig. S7E). This is likely on account of the stronger binding energy between poly-GR and the RNA baits, relative to the binding energy between R-free DPRs and the baits (fig. S7G). The energy is driven by the intermolecular interactions that involve the R-side chains and the phosphate groups of the oligonucleotides (fig. S7H). Critically, these models also demonstrated that the energy of interaction between $(GR)_{50}$ and the 28S rRNA–based bait was higher (>280 kJ/mol) relative to the interaction with the scrambled control bait (fig. S7G), on account of the differential hydrogen bonding between poly-GR

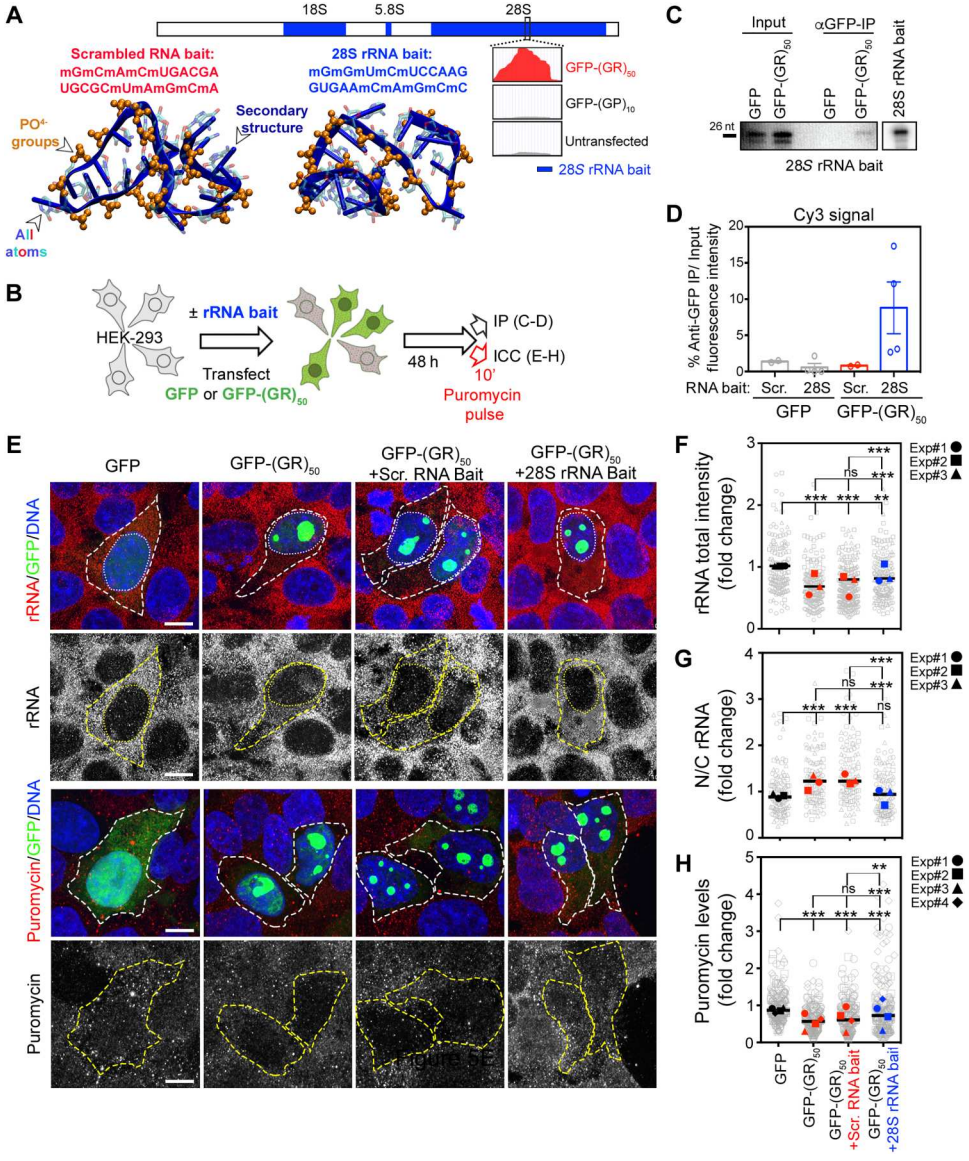

Fig. 6. Modified RNA-based strategy to inhibit the toxic effects of poly-GR on ribosomal homeostasis. (**A**) Top: Schematic representing the enrichment of 28S rRNA in CLIP-Seq analysis and the sequence used to design a "bait" for poly-GR. Bottom: All-atom MD simulation of 28S rRNA and scrambled baits; simplified representation of secondary structure is depicted in blue, PO^{4-} groups in orange, and all atoms in semitransparent multicolor. (**B**) Experimental schematic to assess the interaction with $(GR)_{50}$ and effect of modified 28S rRNA baits in HEK-293 cells. (**C**) Lysates of HEK-293 cells cotransfected with 28S rRNA bait and GFP-$(GR)_{50}$ or GFP and subjected to IP with anti-GFP. RNAs within immunoprecipitates were fractionated in denaturing polyacrylamide/urea gel, and the indicated 28S rRNA bait was detected by NB exclusively in the GFP-$(GR)_{50}$ condition. Input represents 1% of the lysate used in IP. (**D**) Lysates of cells cotransfected with 28S rRNA or scrambled (Scr.) control bait and GFP-$(GR)_{50}$ or GFP and subjected to IP with anti-GFP. Bar graphs showing the level of Cy3-labeled bait detected within the immunoprecipitates normalized to input. (**E**) Confocal images of GFP- and GFP-$(GR)_{50}$–transfected cells immunolabeled for rRNA (top) and puromycin (bottom). Nuclei counterstained with Hoechst 33342. Scale bar, 10 μm. (**F**) Dot plots showing the fluorescence intensity of rRNA in GFP- and GFP-$(GR)_{50}$–transfected cells treated with scrambled or 28S rRNA baits. (**G**) Dot plots showing the N/C rRNA ratio in GFP- and GFP-$(GR)_{50}$–transfected cells treated with scrambled or 28S rRNA–based baits. (**H**) Dot plots showing the fluorescence intensity of puromycin in GFP- and GFP-$(GR)_{50}$–transfected cells treated with scrambled or 28S rRNA baits. In (F) to (H), individual cells from three experiments are represented by distinct shaped symbols in gray, median values of each experiment are represented by distinct shaped symbols in color, and bars represent the global median per condition. Multiple comparisons of means: Tukey contrasts: $^{**}P < 0.01$; $^{***}P < 0.001$.

and the two baits (fig. S7H). This difference is considerable, as according to published work (*46*, *47*), it is enough to drive binding preferences between peptides and chemically similar ligands that have been experimentally defined. Collectively, these simulations predict that the higher-order structure and reduced dynamism of the 28S RNA molecule favor energetically stronger binding to poly-GR compared to the R-free DPRs.

We next sought to support these predictions with experimental data and first confirmed that the 28S bait can interact with synthetic $(GR)_{15}$ but not $(GP)_{15}$ in vitro (fig. S8A). Subsequently, we investigated the specificity of interaction in live transfected mammalian cells (Fig. 6, B to D). IP of GFP or GFP-$(GR)_{50}$ from whole-cell extracts coupled to NB analysis demonstrated a specific interaction between the 28S rRNA–based bait and GFP-$(GR)_{50}$ but not with the GFP control (Fig. 6C). To quantitate the specificity of this interaction in a different way, we cotransfected GFP, GFP-$(GA)_{50}$, or GFP-$(GR)_{50}$ cells with the 28S rRNA–Cy3 bait or the scrambled control–Cy3 molecule. Quantitative measurements of Cy3 fluorescence after precipitation with a GFP antibody demonstrated a specific interaction between GFP-$(GR)_{50}$ and the 28S bait but not with the scrambled control, while GFP or GFP-$(GA)_{50}$ did not exhibit a preferable interaction with either one of the baits (Fig. 6D and fig. S8B).

Next, we delivered the 28S and scrambled control baits to cells expressing GFP or GFP-$(GR)_{50}$ and monitored several metrics related to poly-GR and its adverse effects on ribosomal homeostasis. First, we used confocal imaging to establish that the baits were effectively internalized (fig. S8, C and D) and observed that the 28S rRNA–Cy3 bait exhibited lower total intensity levels (fig. S8E), but significantly higher accumulation in the nucleus of cells expressing GFP-$(GR)_{50}$ relative to cells expressing GFP (fig. S8F), likely on account of the interaction with nuclear poly-GR. Critically, we did not observe any adverse toxic effects in cells treated with either the 28S rRNA–based or scrambled RNA bait (fig. S8G). The 28S rRNA bait resulted in a moderate but significant reduction in the N/C ratio of the GFP-GR signal relative to the untreated poly-GR–overexpressing cells, suggesting that binding to the bait affected the localization of GR (n = 235 cells per condition; $P < 0.05$) (fig. S8H). As we described earlier, cells expressing GFP-$(GR)_{50}$ exhibited a significant reduction in total levels of rRNA [n = 157 cells for GFP, 213 cells for GFP-$(GR)_{50}$; $P < 0.001$] and increased rRNA N/C ratio (n = 114 cells per condition; $P < 0.001$), as well as a decrease in protein translation (n = 188 cells per condition; $P < 0.001$) (Fig. 6, E to H). These deficits were significantly reduced in the presence of the 28S-based bait, which restored rRNA levels [n = 186; $P < 0.001$ relative to untreated GFP-$(GR)_{50}$, and $P < 0.01$ relative to GFP] and subcellular localization [n = 114; $P < 0.001$ relative to untreated GFP-$(GR)_{50}$, and no significant differences relative to GFP], as well as protein translation [n = 188 cells; $P < 0.001$ relative to untreated GFP-$(GR)_{50}$ and GFP], to levels similar to the ones seen in GFP-control cells (Fig. 6, F to H). Moreover, this protective effect was specific to the 28S bait, as its beneficial effects were significantly different relative to cells treated with the scrambled control molecule (n = 269 cells, $P < 0.001$ for total rRNA levels; n = 114 cells, $P < 0.001$ for N/C rRNA ratio; n = 188 cells, $P < 0.01$ for protein translation) (Fig. 6, F to H).

We next interrogated the effects of the 28S bait on a neuronal model of poly-GR toxicity. We differentiated healthy control iPSCs into spinal motor neurons (MNs) using a well-characterized protocol (*48*) and transduced the cultures with a lentivirus expressing GFP or GFP-$(GR)_{50}$. We used live cell imaging analysis to track individual cells over the course of 90 days and found that poly-GR–overexpressing MNs exhibited a moderate but significant reduction in survival relative to GFP-expressing MNs (n = 221 GFP MNs and n = 223 GFP-$(GR)_{50}$ MNs; 8 to 10% reduction, P = 0.0038) (Fig. 7A). All degenerating neurons were characterized by the accumulation of poly-GR–GFP nuclear aggregates, and nuclear aggregation strongly predisposed MNs to degeneration (Fig. 7, B and C). MNs with poly-GR–GFP nuclear aggregates progressively exhibited a significant reduction in total rRNA levels, accumulation of rRNA signal within the nucleus, and reduced protein translation (Fig. 7D and fig. S9, A and B). Administration of the 28S rRNA bait every 28 days in these MN cultures led to a significant increase in survival (Fig. 7E) that was associated with a 46% reduction in MNs with poly-GR nuclear aggregates (Fig. 7F) and a 25% reduction in cell death within MNs with poly-GR nuclear aggregates (Fig. 7G). These results suggest that the 28S bait mitigates toxicity by slowing down the accumulation of toxic nuclear poly-GR. In contrast, the scrambled control had only a minor effect on survival and did not rescue the accumulation of nuclear poly-GR aggregates. The onset of MN death in this cellular model was strictly dependent on the time interval between infection and expression of poly-GR–GFP (fig. S9C).

To assess if the 28S bait can successfully mitigate the toxic effects of the *C9orf72* hexanucleotide repeat expansion (C9-HRE) in a more disease-relevant, physiological system, we used fibroblast-induced MNs (iMNs) (*49*), derived from C9-HRE ALS patients or healthy control subjects (Fig. 8A). In this model system, C9-HRE iMNs degenerate within 2 weeks likely due to a combination of loss-of-function and gain-of-function mechanisms of toxicity associated with the (G_4C_2)-repeat expansion, rather than expression of poly-GR alone (*49*, *50*). Strikingly, administration of single dose of 28S rRNA significantly improved survival and reduced the hazard ratio (*50*, *51*) in iMNs derived from three distinct C9-HRE ALS patients, while the scrambled control RNA had no substantial effect (Fig. 8, B and C).

Last, to assess the ability of the rRNA bait molecule to ameliorate poly-GR toxicity in an intact nervous system in vivo, we used two *Drosophila* models of poly-GR overexpression (Fig. 9 and fig. S10). MN expression of $(GR)_{50}$-EGFP (enhanced green fluorescent protein) is lethal during development, with ~99% of mutant flies dying at pupal stages and failing to eclose (n = 161 flies; Fig. 9, A to D). We reasoned that this highly toxic model would represent a stringent platform to test for any beneficial effects of the modified 28S RNA molecule on GR-DPR toxicity in vivo. We first ensured that the administration of Cy3-conjugated bait in feeding medium during early larval stages led to its sufficient uptake within larval brain cells (Fig. 9, A and B). We found that the 28S rRNA–based bait had no effect on control GFP flies, while it significantly mitigated GR toxicity in $(GR)_{50}$-EGFP mutant flies, with up to 9.3% of animals effectively eclosing and reaching adult stages (Fig. 9D) (n = 151 to 164 flies per group; $P < 0.001$). We obtained similar results using an alternative fly model, where $(GR)_{36}$ is specifically expressed in the fly eye. Treatment with 28S rRNA–based bait had a moderate but highly significant effect, reducing the severity of $(GR)_{36}$-dependent eye degeneration and the appearance of necrotic patches (fig. S10, A to C). Collectively, these experiments demonstrate that administration of a modified 28S rRNA bait

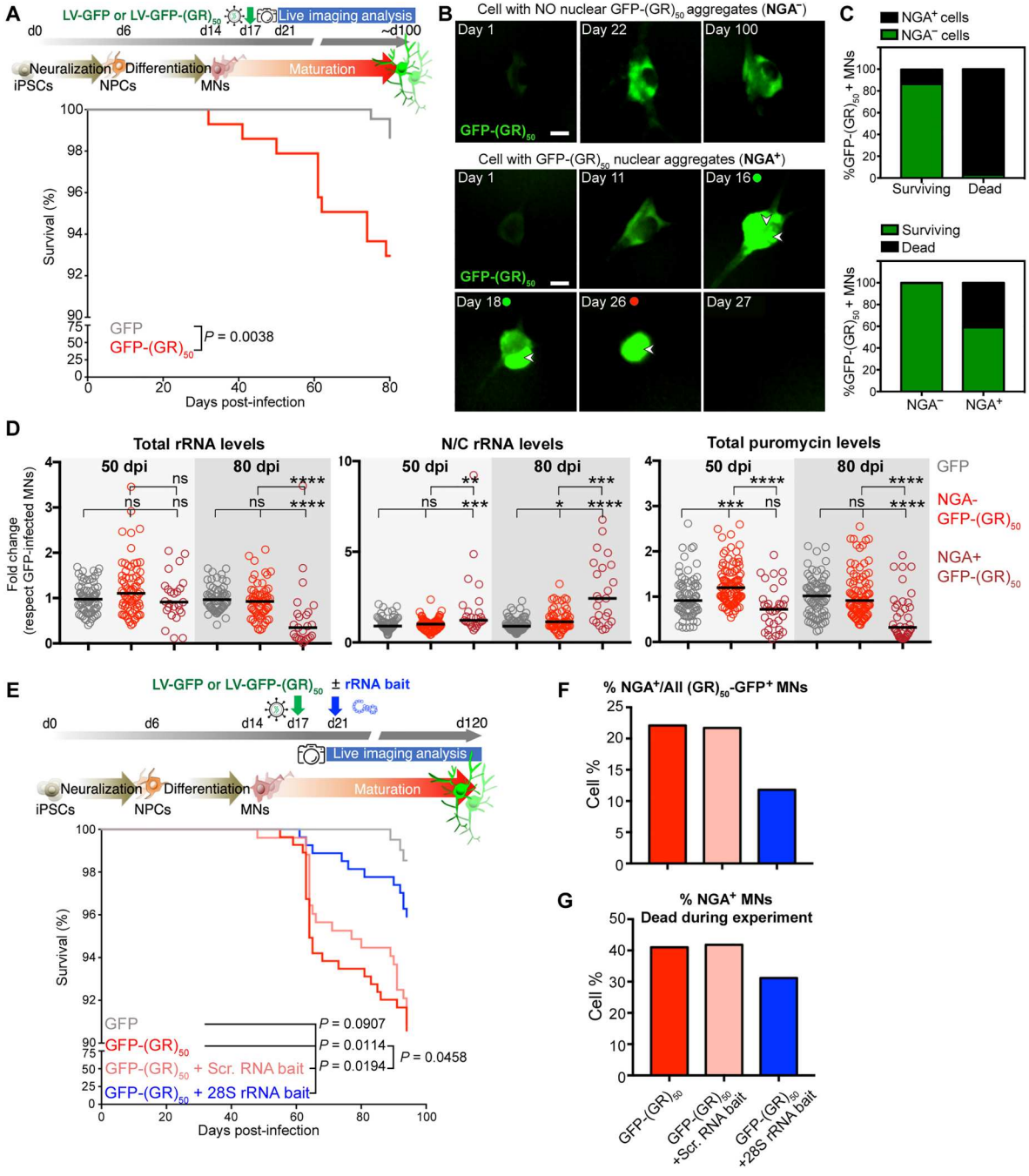

Fig. 7. RNA-based strategy to inhibit the toxic effects of poly-GR in stem cell–derived MNs. (**A**) Top: Experimental workflow with iPSC-derived MNs transduced with GFP or GFP-$(GR)_{50}$ lentiviruses. Bottom: Kaplan-Meier plot displaying survival of iPSC-derived MNs for >80 days after infection (dpi). Traces include neurons from three independent differentiations; n(GFP) = 221 and n(GFP-$(GR)_{50}$) = 223 cells. Statistical comparisons were assessed by Gehan-Breslow-Wilcoxon test; P value displayed in graph. (**B**) Images of GFP-$(GR)_{50}$–transduced MNs with or without nuclear GR aggregates (NGA) at different dpi. Arrowheads indicate NGA. Green or red dots indicate the time at which NGAs appear and MN degenerate, respectively. Scale bar, 10 μm. (**C**) Top: Bar plot showing the percentage of surviving and degenerating GFP-$(GR)_{50}$–transduced MNs, with or without NGAs. Bottom: percentage of GFP-$(GR)_{50}$–transduced MNs with or without NGAs that survive or degenerate. (**D**) Dot plots showing the fold change in total rRNA, N/C rRNA, and puromycin levels in GFP control and GFP-$(GR)_{50}$–expressing MNs, with or without NGA, at 50 and 80 dpi. Each dot represents the value of a single MN. Statistical comparisons were assessed by a Mann-Whitney U test: *P < 0.05; **P < 0.01; ***P < 0.001; ****P < 0.0001. (**E**) Top: Schematic representation of the experimental workflow of iPSC-derived MNs transduced with GFP or GFP-$(GR)_{50}$ lentiviruses and treated with scrambled or 28S rRNA–based baits. Bottom: Kaplan-Meier plot displaying survival of iPSC-derived MNs for all four conditions. Traces include neurons from three independent differentiations: n(GFP) = 206, n[GFP-$(GR)_{50}$] = 276, n(GFP-$(GR)_{50}$ + scrambled bait) = 277, n(GFP-$(GR)_{50}$ + 28S rRNA bait) = 269 cells. Statistical comparisons were assessed by Gehan-Breslow-Wilcoxon test; P values are displayed in the graph. (**F**) Bar plot showing the percentage of MNs that exhibited nuclear GR aggregates (NGA$^+$) over ~90 dpi. (**G**) Bar plot showing the percentage of GFP-$(GR)_{50}$–expressing MNs with or without NGA that degenerated over ~90 dpi.

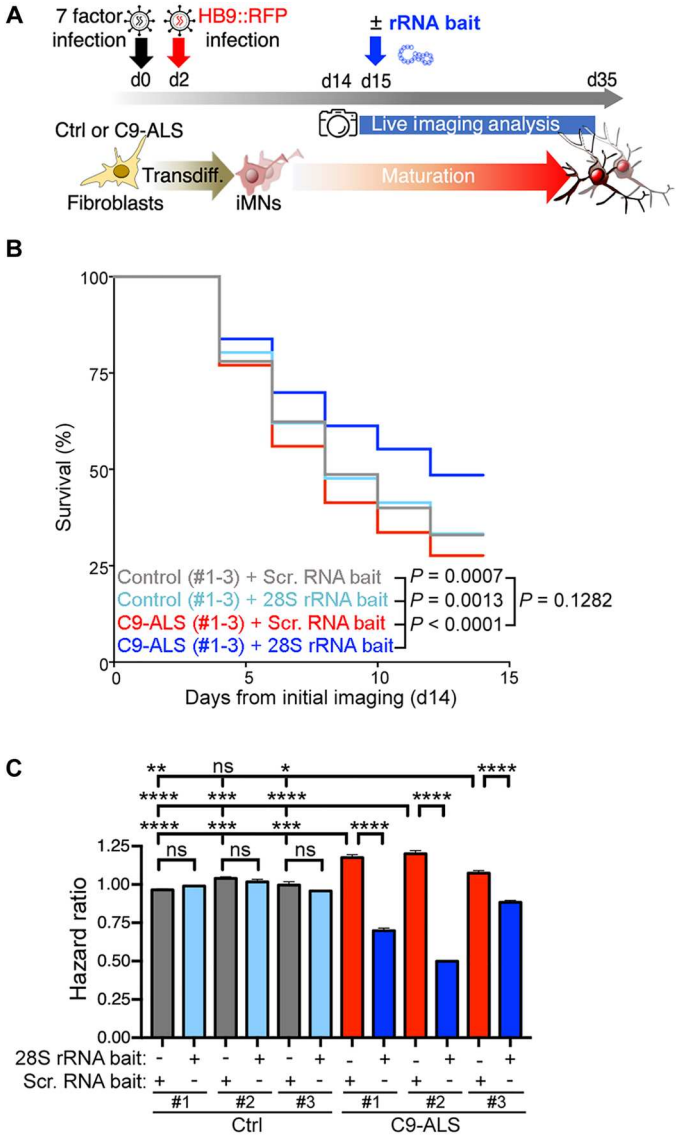

Fig. 8. RNA-based strategy to inhibit the toxic effects of poly-GR in mutant C9orf72 ALS patient iMNs. (**A**) Schematic representation of the experimental workflow for live imaging of induced MNs (iMNs) from three control and three C9orf72-ALS (C9-ALS) patient-derived iPSC lines, which were nontreated or treated with scrambled or 28S rRNA–based baits. (**B**) Kaplan-Meier plot displaying survival of iMNs for all four conditions. Each trace includes neurons from three independent iPSC lines; n = 100 cells per cell line and condition. Comparisons between conditions were assessed by Gehan-Breslow-Wilcoxon test; P values are displayed in the graph. (**C**) Bar plot showing the hazard ratio of three control and three C9-ALS iMNs nontreated or treated with scrambled or 28S rRNA–based baits. The hazard ratio was calculated based on the average of three control lines treated with the scrambled bait. Multiple comparisons by one-way ANOVA followed by Tukey post hoc test: *P < 0.05; **P < 0.01; ***P < 0.001; ****P < 0.0001.

molecule can ameliorate poly-GR–dependent toxicity in multiple model systems in vitro and in vivo.

DISCUSSION

The discovery of C9-HRE as the most prevalent genetic driver of ALS/FTD has stimulated intense interest in deciphering the pathophysiology associated with this mutation. Several studies have shown that C9-DPR proteins have detrimental effects in cellular systems and model organisms (*10*–*20*, *22*). We combined computational and experimental approaches to understand how the interaction of poly-GR with RNA contributes to toxicity. We found that poly-GR directly binds to multiple rRNA species in cells and impedes ribosomal homeostasis. We showcased the strength of the poly-GR/rRNA interaction by using a custom rRNA-based oligonucleotide, which reduced the malignant effects of poly-GR on rRNA levels and localization, protein translation, and toxicity in multiple model systems. Our findings reinforce the importance of ribosomal impairment in C9-ALS/FTD and highlight an innovative approach for protecting against poly-GR pathological mechanisms.

The characterization of the physicochemical features of poly-GR and poly-PR underscored a number of similarities, as well as critical structural differences that likely define their localization, molecular interaction profile, and toxic potential. Although a recent computational study predicts that poly-GR and poly-PR form different oligomers containing what they named double-helix structures (*52*), our analysis consistently shows that poly-GR acquires a random-coiled conformation, while poly-PR is highly enriched in β sheets. The discrepancies between Zheng *et al.* (*52*) and our study are likely driven by the different computational methods. We used continuous MD, which is an unbiased method that models experimental conditions and accounts for the dynamics of the system. Zheng *et al.* (*52*) used discontinuous MD, which favors interactions beyond any unbiased parameterization and thus tends to predict the formation of organized, ordered structures. Further, our computational data were validated by distinct empirical methods that confirmed the different secondary structures predicted for R-DPRs, where the higher rigidity of prolines compared to glycines plays a critical role (*29*). The secondary configuration of poly-PR confers a more stretched conformation, allowing more pronounced exposure of positive charges and a distinct adaptability to interact with complex molecular geometries such as the ones that are required during phase separation (*11*, *28*, *29*, *53*, *54*).

While the size of native DPR proteins produced in physiological models remains unknown, our analysis suggests that their secondary structural features are principally maintained irrespective of repeat number. This is due to the relatively short-range character of the secondary structures that are formed by the DPR amino acids. Several computational studies have demonstrated that sequences of 60 or less amino acids are sufficient for modeling the full conformational space of simple repetitive sequences (*55*, *56*). It is noteworthy that the DPR proteins are unlikely to form a well-defined tertiary structure since at least four distinct amino acids are required for peptide sequences to attain a specific tertiary disposition (*57*, *58*). Thus, our findings support the notion that C9-HRE toxicity is threshold dependent and does not strongly correlate with repeat size (*59*–*63*). At the same time, our conclusions are tempered by the fact that DPRs can be heterogeneous in content (*64*, *65*), while in patients the length of DPRs may be several hundred amino acids longer than the ones we investigated here, and size can affect their subcellular distribution and molecular interactions (*66*).

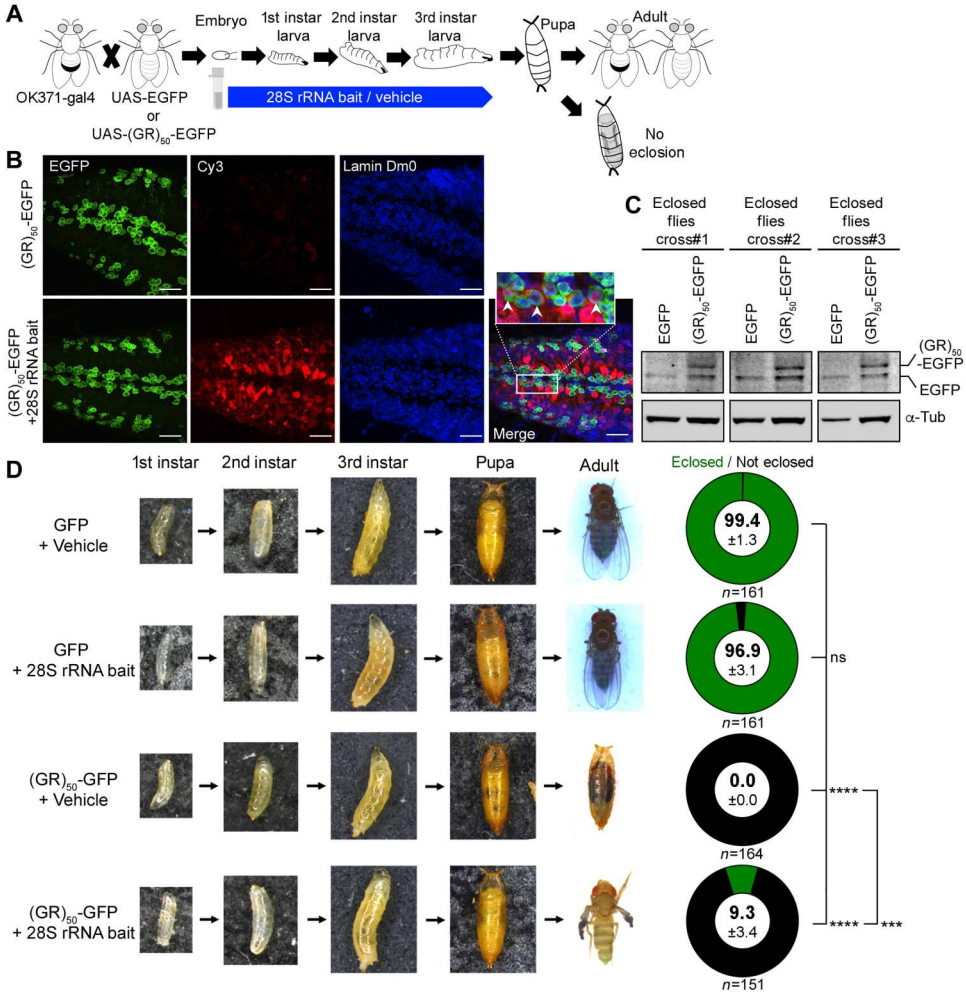

Fig. 9. RNA-based strategy to inhibit the toxic effects of poly-GR in vivo. (**A**) Schematic illustrating a *Drosophila* model to study poly-GR toxicity in the presence or absence of the 28S rRNA–based bait. (**B**) Confocal images showing the GFP and $(GR)_{50}$-GFP transgene expression and the presence of 28S rRNA–based bait conjugated with Cy3 in larval brains. Lamin Dm0 immunolabeling was used as a counterstaining. Arrowheads in merged image insert display the colocalization of $(GR)_{50}$-GFP and 28S rRNA–based bait in larval brain cells. Scale bar, 10 μm. (**C**) Western blot depicting the protein expression of GFP and $(GR)_{50}$-GFP transgenes in brains of flies treated with 28S rRNA–based bait that eclosed. α-Tubulin (α-Tub) was used as a loading control. (**D**) Representative images of larvae, pupa, and adult (OK371-GAL4 × EGFP) or [OK371-GALl4 × $(GR)_{50}$-EGFP] mutant flies in the presence or absence of the 28S rRNA–based bait. Pie charts on the right indicate the percentage of pupae eclosion in the different conditions. Number of animals analyzed per condition is also displayed. One-way ANOVA followed by Tukey post hoc test: ***$P < 0.001$; ****$P < 0.0001$.

Our work demonstrates that poly-GR compromises ribosomal homeostasis and impedes the ability of ribosomes to mediate protein translation. We specifically observed that poly-GR affected the subcellular distribution of rRNA, leading to a high N/C ratio within in vitro models and patient tissue. We hypothesize that this effect is likely the result of poly-GR binding to multiple rRNA species found in both the nucleus and the cytoplasm. This finding is well aligned with previously described defects in ribosomal biogenesis in the nucleus and protein translation in the cytosol (*11*, *16*, *19*, *22*, *24*, *25*, *43*, *67*). Moreover, a recent study demonstrated that C9-HRE patient-derived cells exhibit profound destabilization of ribosomal transcripts (*68*), and we propose that R-DPRs may be contributing to this defect. The shift in rRNA that we observed could also be attributed to a previously described interaction of R-DPRs with nuclear pore proteins (*11*, *17*, *20*, *69*), although the effects of these interactions on N/C transport of rRNA-protein complexes remain unclear (*25*, *70*, *71*).

Postmortem analysis of ALS/FTD patient tissue (*4*, *35*, *36*) and mouse models with C9-GR (*13*, *17*) has shown that the accumulation of poly-GR aggregates in the nucleus is infrequent. While one cannot discount the significance of soluble poly-GR that may exist in the nucleus and may be harder to detect by IHC, our findings provide additional insight to this observation. We found that the nuclear accumulation of poly-GR in human MNs is a rare event (~10% of MNs overexpressing poly-GR exhibit nuclear aggregation), but that nuclear aggregation strongly predisposed MNs to degeneration. Thus, detection of surviving neurons with poly-GR nuclear aggregates postmortem would be rare.

CLIP-Seq analysis revealed that rRNA was the major RNA target of poly-GR in cells. While the potential for R-DPRs to interact with negatively charged molecules such as RNA and DNA had been

established (*21*, *24*, *28*, *29*, *72*, *73*), the identity of interacting RNAs in cells was not known. Our analyses suggest that poly-GR can bind to both immature rRNA species that are found in the nucleolus, as well as fully processed rRNA found within cytosolic ribosomes. The preferential interaction with multiple rRNA species was unexpected, since the physicochemical properties of arginine-rich DPRs as well as the biochemical assays in vitro suggest that they should exhibit rather promiscuous affinity for any available RNA molecule (*73*). However, one should consider that ribosomes are highly abundant in the cell and rRNA is topologically exposed all around the ribosomal surface along with RPs, many of which contain LCDs (table S3) (*74*). This would likely explain the recurrent precipitation of RPs in multiple IP-MS studies (*11*, *15*, *19*, *23*, *27*, *44*). At the same time, our data do not rule out the possibility that poly-GR DPRs recognize specific secondary or tertiary sequence motifs, rather than primary rRNA sequence.

Our dynamic simulations predicted that it is the rRNA that mediates the binding of R-DPRs to the ribosome, at least in the specific region modeled. This region likely represents a physiological binding site as it accommodates both exposed rRNA and RP subunits experimentally shown to bind to poly-GR (*11*, *15*, *19*, *23*, *27*, *44*). However, it is likely that poly-GR interacts with ribosomes at multiple locations. A recent study based on cryo-EM analysis describes the accumulation of short synthetic R-$(DPRs)_{20}$ within the polypeptide tunnel of assembling ribosomes in vitro and suggests that this accumulation perturbs protein translation (*43*). rRNA sequestration and translational stalling caused by the preferential binding of poly-GR to rRNA could be contributing to reported disruptions in nonsense-mediated decay activity in *C9orf72* models (*75*–*77*). Altogether, diverse experimental approaches indicate that R-DPRs can bind to multiple ribosomal regions and at different maturation stages, which cumulatively have a negative impact on ribosomal homeostasis and protein translation (fig. S4E). While our study focused on interactions with RNA, it is noteworthy that other nucleic acids have also been reported to be targeted by R-DPRs, displacing DNA binding factors, impacting chromatin, and eventually affecting multiple cellular functions (*73*).

Our findings showcase the importance of empirical data in cellular context in addition to using in vitro experiments (i.e., purified DPRs with RNA in a test tube). We found that GR exhibited high affinity for tRNAs in vitro, while in live cells, although highly abundant, tRNAs are de-enriched for GR binding. In further support of this argument, Balendra *et al.* (*78*) recently performed similar CLIP-Seq experiments for poly-PR in cells and unexpectedly found that it binds specific mRNAs harboring a GAAGA sequence rather than exhibiting broad unspecific binding to all classes of RNAs (*78*). Further studies, such as the ones performed with other polyamines, including spermine of spermidine (*79*–*81*), are required to determine which RNA properties, e.g., length, sequence, GC content, or secondary structure, among others, might be contributing to the preferential binding of R-DPRs to particular nucleic acids. The high arginine content and AP of R-DPRs differentiate them from polyamines and contribute to their detrimental impact on cellular function. Nonetheless, understanding the unique biophysical properties and pathological effects of these toxic DPRs is crucial for defining their role in neurodegeneration and developing therapeutic interventions.

Research studies around the C9 mutation have highlighted the noncanonical translation of DPR proteins as a pathway that can be targeted therapeutically, and several efforts are focused on identifying the molecular factors that mediate the production of all DPR proteins (*64*, *67*, *82*–*87*). Alternatively, individual DPRs can be targeted by specific antibodies (*88*, *89*) or, as we propose here, by RNA oligonucleotides. The identification of a specific RNA target that natively interacts with poly-GR provided us with an opportunity to design a bait ribonucleotide molecule and assess its ability to protect cells by sequestering away poly-GR from its pathological interactions. The 28S rRNA molecule improved ribosomal homeostasis in $(GR)_{50}$-transfected cells and ameliorated poly-GR toxicity in iPSC-derived MNs overexpressing poly-GR or carrying C9orf72 high-repeat expansions, as well as in a poly-GR *Drosophila* model. However, the phenotypic rescue in the fly is only partial, which could be due to multiple reasons, such as (i) the ability of the 28S rRNA bait to only partially block the association between poly-GR and rRNA, (ii) unbalanced stoichiometry between rRNA and bait, (iii) alternative mechanisms of poly-GR–associated toxicity, or (iv) instability of the bait overtime. Additionally, the true specificity of the 28S rRNA bait toward C9orf72-associated disease mechanisms will be determined in future studies with other ALS animal models and sporadic patient iPSC lines.

The mitigating effects of single-strand RNA and DNA molecules have been explored in the context of other ALS/FTD model systems. Lafarga and colleagues (*73*) showed that noncoding single-strand DNA reduces the toxicity of synthetic R-DPR treatments in U2OS cells and mouse MNs. Similarly, nonspecific sequences of total or noncoding RNA (ncRNA) have been shown to alter the phase transition of C9 R-DPRs (*28*, *72*), as well as to alleviate some of the pathophysiological mechanisms associated with R-DPR overexpression (*71*, *73*). More aligned with the strategy that we propose here, recent studies have shown that short, chemically modified and sequence-specific RNA oligonucleotides of known TDP-43 targets can prevent inclusions and rescue mutant TDP-43 neurotoxicity (*90*). Although more work is required to understand how the binding of the 28S rRNA bait to poly-GR alleviates its pathophysiology, the promising results we present here support the notion that using bait RNAs is useful not only to study RNA-protein interactions (*91*) but also to protect neurons from the detrimental effects of mutant or aberrant proteins (*92*).

MATERIALS AND METHODS

Experimental design

The overall objective of the study is to characterize the interactions of poly-GR with RNA. We describe below the materials, methods, and statistical approaches that we used to execute experiments.

All-atom MD simulations

Peptide structures were built in Avogadro (*93*), and the ribosome structure was obtained from *Oryctolagus cuniculus* (PDB ID: 5LZS) (*45*). Structure prediction of RNA oligonucleotides was performed using two different servers: UNAFold (http://www.unafold.org/) (*94*) and RNAFold (http://rna.tbi.univie.ac.at/cgi-bin/RNAWebSuite/RNAfold.cgi). Outputs obtained from both servers are shown in table S5. The lowest energy results were selected from both methods, and structure comparison revealed that they differed in the intramolecular hydrogen bonding formation by 2 base pairs for the 28S rRNA–based bait and by 1 base pair for the scrambled oligonucleotide. Those with the highest level of order

were chosen for the simulations given that their dynamic nature makes hydrogen bonding creation dependent on conformation probability, while unfavorable interactions break throughout equilibration. Three-dimensional (3D) structures in pdb format were obtained using the RNA composer package (https://rnacomposer.cs.put.poznan.pl/) (*95*). Although the server offers different models to build the 3D structure of RNA from their predicted structure in the Vienna format (table S5), they all came out the same for both RNA oligonucleotides. All MD simulations were carried out in GROMACS 5.0.4 (*96*) using Chemistry at Harvard Macromolecular Mechanics (CHARMM) 36 force field for all-atomistic dynamic simulations that represent all the atoms of the system (*97*–*102*). Force field has been widely used for simulation studies of proteins, peptides, and nucleic acids (*103*–*107*). The experimental system was set up with a constant number of molecules, pressure and temperature, in a 100 mM NaCl environment with TIP3P water (*108*). The simulation box size was set up, allowing a margin of 2 nm at each side of the ribosome, RNA, or stretched DPR. DPR simulations were done for 60 ns. Ribosome was simulated for 100 ns. RNA simulations were run for 120 ns, given that RNAs required conformational reconfiguration from the initial structure. Combined DPR-ribosome systems were set up, placing the equilibrated DPR of 50 repeats close to the area of interest of the equilibrated ribosome, and simulated for 60 ns. Combined DPR-RNA simulations were set up similarly by placing the equilibrated 50-repeat DPRs within interaction distance of the equilibrated scrambled or 28S rRNA baits, and then they were run for 120 ns. Molecular projections do not show the backbone or the hydrogens, which allows a better visualization of the molecular conformation and side chains. However, the multiple calculations considered all the molecular components. All visualizations were rendered using Visual Molecular Dynamics (VMD) package (*109*). The following analyses were also carried out using GROMCAS 5.0.4: R_g (radius of gyration) ≈ peptide extension ≈ 1/folding SASA: Measure the exposure of the molecule to the solvent. AP = SASA(0)/SASA(i); is a normalization to show the tendency of the distinct DPRs to aggregate (AP = 1 means fully soluble, AP > 1 means aggregated).

RMSD (root mean square deviation) measures deviations in the structure with time relative to a reference structure (the initial conformation). Higher RMSD values involve bigger differences with respect to the initial structure. Constant RMSD means stable structures, and hence, reaching a plateau is indicative of equilibrated simulations. RMSF measures the fluctuations of atoms in nanometers relative to a reference structure in a given time range. Measurements through 10 ns in the equilibrated region give a value of the mobility of atoms. Lower RMSF involves lower mobility and, hence, higher stability of the selected atoms in the reference position. Simulation procedure: All the systems were minimized using steepest descent for 50,000 steps or until forces on atoms converged below 1000 pN. The systems were equilibrated in constant number of molecules, volume, and temperature (NVT) ensemble at 300 K for 100 ps, and then in constant number of molecules, pressure, and temperature (NPT) at 300 K and 1 atm for 1 ns, adding constraints in backbone atoms. Simulations were then run for the specified time (100 ns ribosomes and 60 ns DPRs and DPR-ribosome, and 120 ns for RNA and RNA-DPR) systems in NPT ensemble. Equilibrations and simulations used 2-fs time step and periodic boundary conditions in the three spatial coordinates. Verlet cutoff scheme was used for nonbonded interactions with a cutoff radius of 1.2 nm (shifting van der Waals to zero from 1.0 nm) (*110*) and particle mesh Ewald for long-range electrostatics (*111*). Temperature was controlled using velocity rescaling algorithm (τ_T = 0.1 ps) (*112*). Pressure was kept constant using Berendsen algorithm for the NPT equilibration (*113*) and Parrinello-Rahman in the simulations (both τ_P = 2 ps) (*114*).

Coarse-grained MD simulations

APs of the different DPRs were calculated from coarse-grained MD simulations using the MARTINI force field (version 2.2) with coil input secondary structure (*115*–*117*). This model maps up to four heavy atoms to one bead to speed up the simulations. This force field has been previously used to measure peptide AP (*118*, *119*). The result for each DPR is the average of two independent simulations at different simulation box volumes to minimize any finite size effect in the results. Systems were built with constant number of amino acids 1200 or 2400 in a cubic box of 17.1 or 21.6 nm of side, respectively. Final concentrations are 22, 11, 7, and 4 mM for 10, 20, 30, and 50 number of repeats, respectively. Simulation procedure: All systems were minimized using steepest descent for 5000 steps or until forces converged below 200 pN. The systems were equilibrated in NPT ensemble at 303 K and 1 atm for 1000 steps using sequentially 1-, 5-, 10-, and 20-fs time step. Aggregation simulations were then run for 5 μs in the same ensemble with periodic boundary conditions in the three spatial coordinates. A 1.1-nm cutoff was applied for nonbonded interactions using potential shift for Lennard-Jones and reaction field, with a dielectric constant of 15, for electrostatics (*120*). V-rescale and Berendsen algorithms were used to keep temperature (τ_T = 1.0 ps) and pressure (τ_P = 6 ps), respectively, constant (*112*).

Peptide synthesis

Peptides were synthesized via standard 9-fluorenyl methoxycarbonyl (Fmoc) solid-phase peptide chemistry on Wang resin using a CEM Liberty Blue automated microwave peptide synthesizer. Automated coupling reactions were performed using 4 eq of Fmoc-protected amino acid, 4 eq of *N*,*N*′-diisopropylcarbodiimide (DIC), and 8 eq of ethyl(hydroxyimino)cyanoacetate (Oxyma pure), and removal of Fmoc groups was achieved with 20% 4-methylpiperidine in *N*,*N*′-dimethylformamide. Peptides were cleaved from the resin using standard solutions of 95% trifluoroacetic acid, 2.5% water, and 2.5% triisopropylsilane (TIS) and then precipitated with cold ether to yield the crude peptide product. The crude product was purified by preparative reversed-phase high-performance liquid chromatography (RP-HPLC) using a Phenomenex Kinetex column (C_{18} stationary phase, 5 μm, 100 Å pore size, 30 × 150 mm) on a Shimadzu model prominence modular HPLC system equipped with a DGU-20A5R degassing unit, two LC-20AP solvent delivery units, a SPD-M20A diode array detector, and a FRC-10A fraction collector, using H_2O/CH_3CN gradient containing 0.1% (v/v) CF_3COOH as an eluent at a flow rate of 25.0 ml/min.

Liquid chromatography–mass spectrometry

Analytical RP-HPLC was performed at 40°C using a Phenomenex Jupiter 4 μm Proteo 90 Å column (C12 stationary phase, 4 μm, 90 Å pore size, 1 × 150 mm) on an Agilent model 1200 Infinity Series binary LC gradient system, using H_2O/CH_3CN gradient containing 0.1% (v/v) CF_3COOH as an eluent at a flow rate of 50 μl/min. Electrospray ionization mass spectrometry was performed in positive

scan mode on an Agilent model 6510 Quadrupole Time-of-Flight LC/MS spectrometer using direct injection.

Optical density and fluorescence measurements

Optical density measurements were performed on a BioTek model Cytation 3 cell imaging multimode reader. Cytation 3 was also used to quantify fluorescence intensity in cell lysates and immunoprecipitates of HEK-293 cells treated with Cy3-tagged baits.

Circular dichroism

CD spectra were recorded in a Jasco J-815 spectropolarimeter using quartz cells of 100-μm pathlength. Spectra were background-subtracted and are the average of three scans using continuous scanning mode at a speed of 100 nm/min and standard sensitivity. Final spectra are normalized to concentration. Further spectra analysis was carried out using the server BESTSEL (https://bestsel.elte.hu/) (*30*, *31*). Other CD analysis tools were considered, but they were discarded because, unlike BESTSEL, they require the protein family and/or type as input. It is noteworthy that these methods are strongly protein type and parameter dependent, are benchmarked with crystal information, and thus form relatively highly ordered proteins. Additionally, none of the benchmarking sets are expected to have such high percentage of glycine and/or proline as R-DPRs, which can substantially affect the signal. Therefore, the deconvolution results obtained must be taken with caution and only the correlation with other techniques can validate their interpretation. Additionally, the spectra of three reference systems are included. These are a strong β sheet–forming protein, as well as an α helix, and disorder peptide, which are, respectively, UnaG (PDB: 4I3B, 10 μM), consensus tetratricopeptide repeat protein (PDB: 7OBI, 5 μM), and the peptide AAGGEE (50 μM), capped in the N terminus with a palmitic acid and in the C terminus by an amide.

Fourier transform infrared spectroscopy

FTIR spectra were recorded on a Bruker Tensor 37 FTIR spectrometer. Spectra shown are the average of 25 scans with a resolution of 1 cm^{-1}. Samples were prepared in deuterated water (D_2O) to displace its vibrations from the region of interest. Liquid samples were placed between two CaF_2 windows with 50-μm pathlength and background-subtracted using the solvent. Solid FTIR was measured using attenuated total reflectance (ATR) module on lyophilized samples and using background subtraction to remove signals from atmospheric H_2O and CO_2. The liquid FTIR spectra were deconvoluted using Gaussian lineshape to better illustrate the contributions of the different modes (*121*).

RNA-DPR binding assay

The RNA solutions were diluted with Hepes buffer ([phosphate] = 200 μM) and incubated for 30 min at 25°C. A Hepes buffer solution of DPRs (10 mM) was then added to the RNA solutions, and the mixture was pipetted 30 times. Fifty microliters of these suspensions was put into triplicate wells of a 96-well plate, and their optical density at 600 nm was recorded.

Estimation of the content of phosphates in the RNA sample

The content of phosphates in the RNA sample was estimated based on assumptions that the RNA is 100% pure and its counter cation is sodium. Molecular weight of the RNA repeating unit (343.43 g/mol) was calculated by averaging the molecular weights of adenine (351.19 g/mol), guanine (367.19 g/mol), cytosine (327.17 g/mol), and uracil (328.15 g/mol). As the concentration of RNA was shown to be 5.4 μg/μl, the concentration of phosphates was therefore estimated to be 15.7 mM.

Cell culture models

HEK-293FT models

HEK-293FT cells (American Type Culture Collection, RRID: CVCL_6911) were grown in Dulbecco's modified Eagle's medium (DMEM) (Corning) supplemented with GlutaMAX (Gibco) and 10% fetal bovine serum (FBS; Gibco). HEK-293FT cells were dissociated by incubation for 5 min with trypsin-EDTA (Gibco) at 37°C.

iPSC models

The iPSC line (18a: female, 48 years old) derived by retroviral transduction of skin fibroblasts from a healthy control individual (*122*) was used to generate human MNs as described previously (*48*). iPSCs were maintained on Matrigel (BD Biosciences) with mTeSR1 medium (STEMCELL Technologies) and passaged on a weekly basis using 1 mM EDTA or Accutase (Sigma-Aldrich). At 70% confluency, iPSC cultures were dissociated using Accutase and plated at a density of 10^5 cells/cm^2 with 10 μM ROCK inhibitor (Y-27632, DNSK International) in mTeSR1. The next day (day 0), the medium was replaced with N2B27 medium [50% DMEM:F12, 50% Neurobasal, supplemented with nonessential amino acids (NEAAs), GlutaMAX, N2, and B27; Gibco, Life Technologies] containing 10 μM SB431542 (DNSK International), 100 nM LDN-193189 (DNSK International), 1 μM retinoic acid (RA; Sigma-Aldrich), and 1 μM Smoothened agonist (SAG; DNSK International). The culture medium was changed daily until day 6 and then switched to N2B27 medium supplemented with 1 μM RA, 1 μM SAG, 5 μM DAPT (DNSK International), and 4 μM SU5402 (DNSK International). Cells were fed daily until day 14, when MNs were dissociated using TrypLE Express (Gibco, Life Technologies) supplemented with deoxyribonuclease (DNase) I (Worthington) and plated at a density of 10,000 cells per well in the IncuCyte Imagelock 96-well Plate (Sartorius) precultured with 20,000 mouse glial cells per well. Cocultures were feed three times a week with NBM medium (Neurobasal, NEAA, GlutaMAX, N2, and B27) supplemented with 1% FBS, ascorbic acid (0.2 μg/ml; Sigma-Aldrich), BDNF, CNTF, and GDNF (10 ng/ml, R&D Systems).

iMN models

Human lymphocytes from healthy subjects and ALS patients were obtained from the National Institute of Neurological Disorders and Stroke (NINDS) Biorepository at the Coriell Institute for Medical Research and reprogrammed into iPSCs using episomal plasmids as previously described (*49*, *123*, *124*). iPSCs were differentiated into fibroblast-like cells to enable efficient retroviral transduction as described previously (*124*). Reprogramming of fibroblast-like cells was performed in 96-well plates (5×10^3 cells per well) or 13-mm plastic coverslip (3×10^4 cells per coverslip) that had been precoated with 0.1% gelatin (1 hour, room temperature) and laminin (4°C, overnight). Retroviruses encoding seven iMN factors (*Ngn2*, *Lhx3*, *Isl1*, *NeuroD1*, *Ascl1*, *Brn2*, and *Myt1l*) were added in 150 μl of fibroblast medium (DMEM plus 10% FBS) per 96-well with polybrene (8 μg/ml). *Hb9*::RFP (red fluorescent protein) lentivirus was added to the cultures 24 hours after transduction with seven iMN factors. On day 4, primary mouse cortical glial cells isolated from postnatal day 3 ICR pups were added to the transduced cultures in MEM (Life Technologies) and 10% donor

equine serum (HyClone). On day 5, cultures were switched to N3 medium containing DMEM/F12 (Life Technologies), 2% FBS, 1% penicillin/streptomycin, GlutaMAX, N2 and B27 supplements (Life Technologies), 7.5 μM RepSox (Selleck), and 10 ng/ml each of fibroblast growth factor (FGF), glial cell line–derived neurotrophic factor (GDNF), brain-derived neurotrophic factor (BDNF), and ciliary neurotrophic factor (CNTF) (R&D Systems). The cultures were maintained in N3 with neurotrophic factors (RepSox, FGF, GDNF, BDNF, and CNTF) and changed every other day.

Donor information and karyotyping results for iPSCs are displayed in table S6. All cell cultures were maintained at 37°C and 5% CO_2 and tested for mycoplasma monthly.

DPR overexpression in cell culture models

For overexpression experiments, 40% confluent HEK-293 cells were transfected with HilyMax transfection reagent (Dojindo Molecular Technologies) according to the manufacturer's guidelines. Briefly, DNA was mixed with HilyMax (1 μg DNA:3 μl HilyMax ratio) in Opti-MEM (Gibco) and incubated for 15 min at room temperature before being added to cells. Cells were incubated with transfection mixture for 4 hours at 37°C, and then the medium was replaced. Analyses made on transfected cells were performed 48 to 72 hours after transfection.

Overexpression of GFP or GFP-$(GR)_{50}$ in iPSC-derived MNs was achieved through lentiviral infection. MNs were infected with lentiviral stocks for 24 hours on day 17 of differentiation. We performed real-time quantitative live-cell imaging analysis using the IncuCyte Live-Cell Analysis System as well as immunocytochemistry at multiple time points.

iMN survival assay

Transfection was performed on day 15 of the iMN conversion assay. The next day, a complete medium change without RepSox, FGF, GDNF, BDNF, or CNTF was done and longitudinal tracking of iMNs was initiated. Images of Hb9::RFP^+ iMNs were taken using Molecular Devices ImageExpress once every other day for 14 days. Tracking of neuronal survival was performed using SVcell 3.0 (DRVision Technologies) or ImageJ. Neurons were scored as dead when their soma was no longer detectable by RFP fluorescence.

Plasmids and virus stock preparation

HEK-293 cells were transfected with the pcDNA3.1 plasmid containing GFP, GFP-$(GP)_{10}$, or GFP-$(GR)_{50}$, in which alternative codons were used to generate DPRs without generating the $(GGGGCC)_n$ transcript. These constructs were made and kindly shared by the Petrucelli laboratory (*125*). We resorted to using a GFP-$(GP)_{10}$ expression plasmid because the GFP-$(GP)_{50}$ version was unstable and retracted to smaller sizes during bacterial expansion. iPSC-derived MNs were transduced with lentivirus containing the abovementioned GFP or GFP-$(GR)_{50}$ sequences inserted in the lentivector backbone CD510B. Packaging from lentiviral constructs was performed in HEK-293FT cells by transfecting packaging components contained in pMD2.G and psPAX2 vectors with HilyMax (Dojindo Molecular Technologies). Virus was collected from cell medium 48 to 96 hours after transfection. Lentiviral concentrated stocks were obtained after filtering collecting medium and centrifugation at 25,000*g* for 2 hours at 4°C.

For iMN models, the cDNA for each iMN factor (*Ngn2*, *Lhx3*, *Isl1*, *NeuroD1*, *Ascl1*, *Brn2*, and *Myt1l*) was purchased from Addgene and cloned into the pMX retroviral expression vector using Gateway cloning technology (Invitrogen). The Hb9::RFP lentiviral vector and rtTA3 lentiviral vector were also purchased from Addgene (ID: 37081; 61472). Viruses were produced as follows. HEK-293T cells were transfected in a 10-cm dish at 80 to 90% confluence with viral vectors containing each iMN factor and viral packaging plasmids (PIK-MLV-gp and pHDM for retrovirus, pPAX2 and VSVG for lentivirus) using polyethylenimine (PEI) (Sigma-Aldrich). The medium was changed 24 hours after transfection. Viruses were harvested at 48 and 72 hours after transfection. Viral supernatants were filtered with 0.45-μm filters, incubated with Lenti-X concentrator (Clontech) for 24 hours at 4°C, and centrifuged at 1500*g* at 4°C for 45 min. Pellets were resuspended in DMEM plus 10% FBS (200 μl per 10-cm dish of HEK293T) and stored at −80°C.

CLIP sequencing

CLIP experiments were performed as described (*41*). Briefly, cells were crosslinked in a Spectroline UV crosslinker using UVC (100 mJ/cm^2, 254 nm). Cells were lysed in 50 mM tris-HCl (pH 7.4), 150 mM NaCl, 1% NP-40, 0.5% sodium deoxycholate, 0.1% SDS with EDTA-free complete mini protease inhibitor cocktail (Roche), and 1 mM phenylmethylsulfonyl fluoride (PMSF). After sonicating on ice using a Branson sonifier, lysates were incubated with Turbo DNase (4 U/ml) (Invitrogen) and RNase I (0.2 to 0.002 U/ml) (Invitrogen). IP was performed by incubating the lysates with GFP-Trap Magnetic beads (Chromotek, catalog: gtd-10, RRID: AB_2827592) for 1.5 hours at 4°C. Afterward, beads were washed twice with high-salt buffer [50 mM tris-HCl (pH 7.4), 1 M NaCl, 1% NP-40, 0.5% sodium deoxycholate, 0.1% SDS] and twice with T4 Polynucleotide Kinase (PNK) buffer [20 mM tris-HCl (pH 7.4), 10 mM $MgCl_2$, 0.2% Tween 20]. RNA 3′ ends were dephosphorylated with PNK as described (*41*), followed by two washes each with high-salt and PNK buffers. 3′ Linker ligation was performed on beads overnight at 16°C followed by two additional washes each with high-salt and PNK buffer. After labeling with [γ-^{32}P]ATP (adenosine triphosphate) and T4 RNA ligase, ribonucleoproteins (RNPs) were resolved on NuPAGE 4 to 12% bis-tris gels (Invitrogen) run in NuPAGE Mops-SDS running buffer (Invitrogen). After gel fractionation, RNPs were transferred to Amersham Protran 0.45-μm nitrocellulose membranes (Cytiva) and labeled complexes were visualized using a storage phosphor screen and developed on a Typhoon FLA 9000 scanner. RNA-protein complexes of the expected size were excised from the nitrocellulose membranes, along with the same size region from GFP, GFP-$(GP)_{10}$, or untransfected control experiments. Associated proteins were removed by digesting with proteinase K [(PK) 1 mg/ml)] (Invitrogen) for 20 min at 37°C in PK buffer [100 mM tris-HCl (pH 7.4), 50 mM NaCl, 10 mM EDTA] followed by a second digestion for 20 min at 37°C in the presence of 3.5 M urea. Afterward, RNA was extracted with phenol/chloroform and reverse transcription was performed using SuperScript III (Invitrogen) using the following primers: library 1 GFP—Rt1clip, GFP-$(GR)_{50}$—Rt6clip; library 2 untransfected—Rt1clip, GFP-(GP)10—Rt6clip, GFP-$(GR)_{50}$—Rt9clip. cDNA was size-selected and circularized with Circligase II (Epicentre). Circularized cDNA was cut with Bam HI and amplified using Accuprime Supermix I (Invitrogen). The PCR cycle number was optimized to prevent overamplification of the library.

Amplified samples were sequenced on the Illumina MiSeq platform in single end read mode with 110-nt reads.

CLIP-Seq bioinformatics

For mapping to the whole genome, barcoded sequencing libraries were demultiplexed, allowing 1-nt barcode mismatch, and adapter sequences and low-quality bases were filtered using iCount (version 2.0) (https://github.com/tomazc/iCount). Trimmed, single-end reads were aligned to the hg38 genome (Gencode V32) using Novoalign (version 4.03.03). Parameters for alignment included the following: score threshold (-t) set to 15,3, the minimum number of bases for alignment (-l) set to 20, the gap penalty (-x) set to 4, gap opening penalty (-g) set to 20, trimming step size (-s) set to 1, score difference (-R) set to 0, and multimapping reporting (-R) set to ALL. The quality of the sequenced libraries was assessed per sample using FastQC (version 0.11.5) (https://www.bioinformatics.babraham.ac.uk/projects/fastqc/), FastQ Screen (version 2) (*126*), and samtools (version 1.13) (*127*). Samples were deduplicated using UMI-tools (*128*), with multimapping detection. On average, 5.33 unique molecular identifiers (UMIs) were detected per position.

To determine the location of CLIP peaks, overlapping reads were collapsed to create a list of genomic regions using bedtools (version 2.30.0) (*129*). Peaks found within 50 nt of one another were combined to a single feature. Reads associated with CLIP peaks were counted using FeatureCounts (version 2.0.2) (*130*) with the following parameters: The number of reads supporting each exon-exon junction was included, the minimum number of overlapping bases in a read required for assignment was 1, and strand-specific read counting was performed. Analysis was performed without multimapped reads (unique reads only) and with multimapped reads included (unique + multimapped reads). Multimapped reads were assigned a fractional count of $1/x$, where x is the total number of alignments reported for the same read. CLIP peaks with >5 unique + fractional multimapped reads were annotated with overlapping genomic features. Protein coding and ncRNA features were identified from the Gencode hg38 V32, while ncRNA and repeat regions were identified from hg38/GRCh38 Repeatmasker annotations and rRNA annotations were identified from RefSeq GRCh38.p13 (GCF_000001405.39). All features annotated for each peak are reported in table S2. Representative peaks with multiple annotations were initially examined manually to determine the correctness of the annotations. On the basis of this analysis, preference was given to annotations as follows: rRNA > ncRNA > protein coding: exon > repeat element > pseudogene > lncRNA: exon > antisense feature > protein coding: intronic > lncRNA: intronic > no feature.

To identify specific sites of RNA binding, MAnorm (version 1.1.4) (*131*) was used to identify enriched CLIP peaks in GFP-$(GR)_{50}$ versus GFP samples. Default parameters were used except for the following: Shift size for both inputs (--s1,--s2,) was set to 0 to keep the peak binding site at the 5′ end, and the summit-to-summit distance cutoff for common peaks (-d) was set to 25 to ensure that only overlapping peaks between samples were compared. Ten thousand simulations (-n) were performed to test enrichment. CLIP peaks with a fold change of >2 and a P value of <0.05 were identified as significant binding events.

For mapping to the RNA45SN1 locus, PCR duplicates were removed by collapsing identical sequences using the FastX_collapser. PhiX spike in control reads was removed by mapping to Coliphage phi-X174, complete genome (NCBI reference sequence: NC_001422.1). The remaining reads were demultiplexed based on barcodes using FastX_splitter, and then adapter and UMI sequences were removed with fastX_trimmer and fastX_clipper, respectively (Fastxtoolkit version 0.0.14) (http://hannonlab.cshl.edu/fastx_toolkit/). Bowtie2-build was used to generate a genomic index from the RNA45SN1 (NC_000021.9) sequence. Reads were mapped to this index using Bowtie2 (version 2.4.4) (http://bowtie-bio.sourceforge.net/bowtie2/index.shtml) with the --very-sensitive-local option. Unmapped reads were extracted using Samtools-view and mapped to the hg38 human genome using STAR. Reads mapping to 45S were counted based on the regions with which they overlapped. Bedtools intersect was used to count reads in the various regions. For precursor regions (5′ETS, ITS1, ITS2, and 3′ETS), reads with at least 1 nt in these regions were counted. For mature rRNA regions (18S, 5.8S, and 28S), only reads mapping entirely within these regions were counted. The percentage of reads mapping to each region were represented as a percentage of the total collapsed read number.

To compare our rRNA reads to those present in other iCLIP datasets, fastq files for YTHDC2 iCLIP (SRR3175596) and HNRNPA1 iCLIP (ERR908337) were obtained from the NCBI Sequence Read Archive (SRA). Fastq files were mapped to the hg38 genome using STAR and demultiplexed using UMItools. Bedgraph files of the reads mapping to rRNA at chr21:8,436,754-8,446,360 were generated using Bedtools and normalized by the total number of reads mapping to this region in each library.

RIP followed by detection of RNAs by NB or RT-qPCR

HEK-293 cells expressing GFP- or GFP-$(GR)_{50}$ were lysed in NET-2 [50 mM tris (pH 7.5), 150 mM NaCl, 2.5 mM $MgCl_2$, 0.5% NP-40] and 1 mM phenylmethylsulfonyl fluoride (PMSF). After sonicating in a Bioruptor Plus on high (30 s on, 30 s off) for 1 min at 4°C, lysates were sedimented at 16,000g for 10 min. Cleared lysates were incubated with 25 μl of GFP-Trap magnetic beads for 1.5 hours at 4°C with rotation. Beads were washed twice in NET-2, transferred to a fresh tube, and washed two additional times. Beads were resuspended in 400 μl of NET-2 and extracted with an equal volume of acid-phenol:chloroform (Invitrogen AM9722). After centrifugation at 16,000g for 15 min, RNA was precipitated from the aqueous phase by adding $^1/_{10}$th volume sodium acetate and 2.5 volumes 100% ethanol. After precipitation, RNA was fractionated in a 5% polyacrylamide/7 M urea gel (to detect RNAs of less than 500 nt) or an 0.8% agarose/formaldehyde gel using the tricine/triethanolamine buffer system described by (*132*) to detect larger RNAs. RNA was transferred from polyacrylamide gels to Hybond-N (Cytiva) in 0.5× Tris-Borate-EDTA (TBE) for 16 hours at 150 mA. RNA was transferred from agarose gels to Hybond-N by capillary transfer overnight using 10× SSC [1.5 M NaCl, 150 mM sodium citrate (pH 7)]. RNA was crosslinked to membranes using a Spectroline UV crosslinker and hybridized in modified (*133*) hybridization buffer [1% bovine serum albumin (BSA), 2 mM EDTA, 200 mM $NaHPO_4$ (pH 7.2), 15% deionized (DI) formamide, 7% SDS] using 5′-^{32}P–labeled oligonucleotides at 28°C. NB probe sequences used in this study: 5.8S, GTGTCGATGATCAATGTGTCCTGCAATTCA; 18S, CGCTCCACCAACTAAGAACG; 28S, CCTGGTTAGTTTCTTCTCCTCC; 7SL, CCATATTGATGCCGAACTTAGTGC; RPPH1,

CTGTTCCAAGCTCCGGCAAA and AATGGGCGGAGGAGAGTAGT.

For RT-qPCR analyses, the RNA was reverse-transcribed using the iSCRIPT cDNA Synthesis Kit (Bio-Rad) and qPCR was performed using iTaq Universal SYBR Green Supermix (Bio-Rad). Samples were run on the Bio-Rad CFX96 Real Time PCR System and analyzed using Maestro software (Bio-Rad).

Primer sequences used in this study: 28S_F, GGAGGAGAAGAAACTAACCAGG; 28S_R, GTCTTCCGTACGCCACATGTC; 18S_F, CTCAACACGGGAAACCTCAC; 18S_R, CGCTCCACCAACTAAGAACG; 5′ ETS_F, TCTAGCGATCTGAGAGGCGT; 5′ ETS_R, CAGCGCTACCATAACGGAGG; ITS1_F, CAACCCCCTCTCCTCTTGGG; ITS1_R, GAGGTCGATTTGGCGAGGG; Y4_F, GGCTGGTCCGATGGTAGTGG; Y4_R, AAAGCCAGTCAAATTTAGCAGTGGG; Y5_F, AGTTGGTCCGAGTGTTGTGGG; Y5_R, AAAACAGCAAGCTAGTCAAGCGCG; tRNA-Glu_F, TCCCACATGGTCTAGCGG; tRNA-Glu_R, TTCCCACACCGGGAGT.

IP followed by NB or fluorescence intensity analysis to detect bait RNA

GFP-GR_{50}– and bait-transfected HEK293 cells were lysed with NET-2 buffer (50 mM tris, 150 mM NaCl, 2.5 mM $MgCl_2$, 0.5% NP-40) supplemented with protease inhibitors. Samples were sonicated at 4°C using Bioruptor Pico (Diagenode B01080010) on high mode, 30 s on and 30 s off for two cycles. Lysates were cleared by centrifugation at 16,000*g* for 10 min at 4°C. Supernatants were incubated with GFP-Trap magnetic beads (Chromotek gtd-10) at 4°C for 90 min using manufacturer recommended guidelines. The bead-sample complex was washed twice with NET-2, moved to a new tube, and washed two more times.

For NB analysis, beads were resuspended in 400 μl of NET-2 and extracted with an equal volume of phenol:chloroform:isoamyl 25:24:1 (Invitrogen, 15593031). After centrifugation at 16,000*g* for 15 min, RNA was precipitated from the aqueous phase by adding sodium acetate to 0.5 M and 2.5 volumes 100% ethanol and incubating overnight at −20°C. After precipitation, RNA was fractionated in an 8% polyacrylamide/7 M urea gel. RNA was transferred from the polyacrylamide gel to Hybond-N (Cytiva) in 0.5× TBE for 1.5 hours at 250 mA at 4°C. RNA crosslinking to Hybond-N was performed as described (*134*), incubating the membrane with chemical crosslinker at 60°C for 1 hour. Hybridization was performed in 1% BSA, 1 mM EDTA, 500 mM $NaHPO_4$ (pH 7.2), and 7% SDS (*133*) using ^{32}P-labeled oligonucleotides at 28°C.

For fluorescence-based analysis of the interaction of Cy3-labeled rRNA baits with poly-GR, following the fourth wash of NET-2, the bead-sample complex was eluted with 2% SDS solution and incubated at 95°C for 10 min. Cy3 dye signal in the respective input cell substrates and eluted products, which results from the magnetic-based IP, was analyzed in a Cytation 3 automated fluorescence plate reader (BioTek).

3′ RACE and SB

RNA was collected as described for RIP RT-qPCR. A 5′ adenylated, 3′ blocked DNA oligonucleotide adaptor (rApp-AGATCGGAAGAGCGGTTCAG-ddC) was ligated to IP and input RNA with T4 RNA ligase for 1 hour at 28°C, 6 hours at 25°C, and 6 hours at 22°C in a 20-μl reaction containing 2 μM adaptor. Adaptor ligated RNA was purified from free adaptor using Dynabeads MyONE Silane (Thermo Fisher Scientific, 37002D). Following elution of adaptor-ligated RNA from MyONE Silane beads, reverse transcription was performed with SuperScript III reverse transcriptase (Thermo Fisher Scientific, 18080093) using 0.5 pmol of reverse transcription (RT) oligo (GGATCCTGAACCGCT) in a 20-μl reaction. RNA in the RT reaction was hydrolyzed by adding 1.65 μl of 1 M NaOH and incubating at 98°C for 20 min. RT products were then purified with a second round of MyONE Silane bead purification. The 3′ end of 18S RNA was PCR-amplified using Phusion HF master mix (Thermo Fisher Scientific, F531L) in a 40-μl reaction containing 0.5 μM primers (18S 3′ end: GCTGAGAAGACGGTCGAACTTGAC and adaptorRev: CTGAACCGCTCTTCCGATCT) and half of the purified RT product. PCR was performed using the following thermocycler program for 24 cycles: 98°C for 10 s, 65°C for 30 s, 72°C for 30 s, with a final 3-min extension at 72°C. PCR products were separated on a 1× TBE and 3% Agarose, Supra Sieve GPG gel for 2 hours at 150 V. Gel was soaked in denaturing buffer (1.5 M NaCl, 0.4 M NaOH) two times for 10 min followed by neutralizing buffer [0.5 M tris (pH 6.5), 2.5 M NaCl] for 10 min. After transferring the DNA to Hybond-N+ membrane by capillary transfer in 20× SSC overnight, the membrane was baked at 80°C for 2 hours. Radiolabeling and probing were performed as described in NB methods. Probe sequences: 18S 3′ extended precursor—CGGGCTCCGTTAATGATCCT; 18S mature 3′ end —GCAGGTTCACCTACGGAAAC.

IP followed by Western blot or fluorescence intensity analysis

Cells were harvested in IP buffer [10 mM Hepes (pH 7.6), 100 mM NaCl, 1 mM EDTA, 1 mM NaF, 2 mM Na_3VO_4, 1 mM dithiothreitol (DTT), 1 mM PMSF, 1% sodium deoxycholate, 10% glycerol, 0.1% SDS, 1% Triton X-100, and 1× protease inhibitor cocktail]. Lysates were sonicated, and protein concentrations were determined with a BCA kit (Pierce). GFP and GFP-tagged proteins were immunoprecipitated from 1 mg of protein/sample with anti-GFP antibody (Abcam, RRID: AB_305643). IP of the target antigen was performed using Dynabeads Protein A (Novex, Life Technologies) following the manufacturer′s protocol. Eluted proteins were separated by SDS-PAGE followed by electrotransfer to a nitrocellulose membrane (Bio-Rad). The membranes were blocked in tris-buffered saline (TBS; 50 mM tris, 150 mM NaCl, HCl to pH 7.6) + 0.1% Tween 20 (Bio-Rad) + 5% nonfat dry milk (LabScientific) and incubated overnight at 4°C with primary antibodies: glyceraldehyde-3-phosphate dehydrogenase (GAPDH) (rabbit, 1:1000, Cell Signaling, RRID: AB_561053), GFP (goat, 1:1000, Abcam, RRID: AB_305643), and RPL7A (rabbit, 1:1000, Cell Signaling Technology, RRID: AB_2182059). Primary antibodies were diluted in TBS + 0.1% Tween + 5% BSA (Calbiochem). After several washes in TBS + 0.1% Tween, membranes were incubated with their corresponding secondary anti-rabbit and anti-mouse horseradish peroxidase (HRP)–-conjugated antibodies (1:5000, LI-COR Biotechnology, RRID: AB_2721264, RRID: AB_2721263). Protein signals were detected by ChemiDoc XRS+ (Bio-Rad), using the SuperSignal West Pico chemiluminescent system (Thermo Fisher Scientific).

Immunocytochemistry

Cells were fixed with 4% paraformaldehyde for 20 min, washed with phosphate-buffered saline (PBS), and permeabilized/blocked for 1 hour in PBS containing 10% normal donkey serum (Jackson

ImmunoResearch) and 0.2% Triton. Samples were then incubated overnight at 4°C with primary antibodies: puromycin (mouse, 1:5000, Millipore, RRID: AB_2566826), rRNA (mouse, 1:1000, Novus Biologicals, RRID: AB_10000550), fibrillarin (rabbit, 1:2000, Abcam, RRID: AB_2105785), and NPM1 (mouse, 1:500, Santa Cruz Biotechnology, RRID: AB_628035). The next day, PBS + 0.1% Triton was applied for several washes. Samples were then incubated with the appropriate secondary antibodies conjugated to Alexa Fluor 488 (anti-mouse: AB_141607; anti-rabbit: AB_2535792), Alexa Fluor 555 (anti-mouse: AB_2536180; anti-rabbit: AB_162543), or Alexa Fluor 647 (anti-chicken: AB_2340380) fluorophores (1:500 to 1:1000, Molecular Probes) for 1 hour at room temperature. Cell nuclei were labeled using Hoechst 33342 (Life Technologies) to stain DNA. Immunolabeled samples were blinded upon mounting for subsequent imaging analysis.

Immunohistochemistry

Immunohistochemistry was performed on postmortem motor cortex samples from three ALS patients carrying C9-HRE mutations and three nonneurological controls, obtained through the Northwestern University ALS Clinic, using previously described methods (*135*). Written informed consent and agreement to enter the brain donation program were obtained from all participants in the study, and the study was approved by the Northwestern University Institutional Review Board and in accordance with the Helsinki Declaration (www.wma.net/en/30publications/10policies/b3/). Briefly, 6-μm sections were cut from formalin-fixed and paraffin-embedded brain regions containing motor cortex. Sections were deparaffinized and rehydrated in serial solutions: 3 × 10 min in xylene, 3 × 5 min in 100% ethanol, 3 × 3 min in 95% ethanol, 1 × 5 min in 75% ethanol, 1 × 5 min in 50% ethanol, 1 × 5 min in deionized water, and 1 × 5 min in PBS. Antigen retrieval was performed using a decloaking chamber with Antigen Decloaker solution (Biocare Medical) at 125°C for 10 min. Sections were cooled to room temperature for 30 min and rinsed with deionized water. Samples were blocked with 1% BSA in PBS for 20 min at room temperature and subsequently incubated overnight at 4°C with primary antibodies: rRNA (mouse, 1:250, Novus Biologicals, RRID: AB_10000550) and MAP2 (chicken, 1:500, Abcam, RRID: AB_2138153). We next rinsed 3 × 5 min with PBS and incubated with appropriate secondary antibodies conjugated to Alexa Fluor 488 or Alexa Fluor 647 fluorophores (1:250, Molecular Probes) at room temperature for 45 min. Slides were rinsed 3 × 5 min, and cell nuclei were labeled by DNA staining using Hoechst (Life Technologies) for 30 min at room temperature. To diminish autofluorescence, 0.3% Sudan black in 70% ethanol was applied to each section for 45 s and rinsed in deionized water for 5 min. Slides were mounted in ProLong Diamond Antifade Mountant (Thermo Fisher Scientific), and labels were blinded for subsequent image analysis.

De novo protein translation analysis

For single-cell protein translation analysis, we used a puromycin-based method termed SUnSET (*136*) that labels newly synthesized proteins. In short, cell cultures were pulsed for 5 to 10 min with puromycin (20 μM) at 37°C. Cells were then fixed, and immunocytochemistry with anti-puromycin antibody was carried out as described above.

rRNA bait design

We design 20-nt RNA baits based on the $(GR)_{50}$-interacting 28S rRNA sequence identified by CLIP-Seq (Fig. 3). We introduced 2′-*O*-methylations in the five nucleotides at the 5′ and 3′ ends to improve their stability (mGmGmUmCmUrCrCrArArGrGrUrGrArAmCmAmGmCmC). Using the same numbers of each of the four ribonucleotides, we designed a scrambled sequence through the InvivoGen webtool https://www.invivogen.com/sirnawizard/scrambled.php.(mGmCmAmCmUrGrArCrGrArUrGrCrGrCmUmAmGmCmA). RNA baits were delivered with Lipofectamine RNAiMAX Transfection Reagent in Opti-MEM (Invitrogen) for 24 hours following the manufacturer's instructions. To evaluate cellular internalization of the RNA baits, we added a Cy3 fluorophore at the 3′ end of the ribonucleotide (mGmGmUmCmUrCrCrArArGrGrUrGrArAmCmAmGmCmC/3Cy3Sp/). All the RNA oligonucleotides used in this study were synthesized by Integrated DNA Technologies.

Drosophila stocks

Drosophila melanogaster's strains GMR-gal, W1118, UAS-EGFP, UAS-FLAG-GR50-EGFP, and UAS-GR36 were used to assess poly-GR toxicity and the potential blocking effect of 28S rRNA bait in vivo. Transgenic flies were generated as previously described for other *C9orf72* DPR fly models (*12*, *16*). Fly stocks and crosses were maintained on standard fly medium in light/dark controlled incubators. We used both males and females, and analyses were done at larvae and adult stages. The fly strains used in the current study are freely available upon request.

Drosophila larval eclosion assay

UAS-EGFP and UAS-FLAG-GR50-EGFP lines were crossed with the MN driver OK371-GAL4 on food mixed with and without 5 μM RNA bait and incubated at 18°C. RNA bait concentration (5 μM) was determined from (*137*). The larvae were closely monitored from the first instar stage until they eclosed and become adults. The images of each developmental stage were taken using a Leica M205C dissection microscope equipped with a Leica DFC450 camera. Eclosion percentages were calculated as follows: (total number of eclosed adults)/(total number of pupal cases) × 100. Each condition was analyzed in triplicate using biological replicates.

Drosophila eye degeneration assay

UAS-GR36 virgin females were crossed with GMR-GAL4 males on food mixed with and without 5 μM RNA bait and incubated at 25°C. Adult eyes were imaged with a Leica M205C microscope 0 to 1 days after eclosion. Images of external eye phenotypes were then scored as previously described (*138*, *139*). Briefly, eyes were examined for the presence or absence of the following features: supernumerary inter-ommatidial bristles, abnormal bristle orientation, ommatidial fusion, ommatidial pitting, disorganization of ommatidial array, and retinal collapse. If the following features were present, one point was given. Additional points were added corresponding to the total percentage of the effected eye area.

Drosophila Western blot

Adult fly heads were collected from EGFP and FLAG-GR50-EGFP flies on RNA bait food that eclosed and snap-frozen on dry ice. Heads were crushed on dry ice and incubated in RIPA buffer (150 mM NaCl, 1% NP-40, 0.1% SDS, 1% sodium deoxycholate,

50 mM NaF, 2 mM EDTA, 2 mM DTT, 0.2 mM Na orthovanadate, 1× Roche protease inhibitor #11836170001). Lysates were sonicated and centrifuged to remove debris. Supernatants were boiled in Laemmli buffer (Boston Bioproducts, #BP-111R) for 5 min and loaded onto 4% to 12% NuPAGE bis tris gels (Novex/Life Technologies). Proteins were transferred using iBlot2 (Life Technologies, #13120134) onto nitrocellulose (iBlot 2 NC regular Stacks, Invitrogen, #IB23001). Western blots were blocked with milk solution (BLOT-QuickBlocker reagent, EMB Millipore, #WB57-175GM) and incubated with primary antibody overnight: chicken anti-GFP antibody (1:3000, Abcam) and mouse anti-tubulin (1:10,000, Sigma-Aldrich). Blots were washed and incubated in secondary antibody for 1 hour [anti-mouse IRDye 680D, 1:10,000 (LI-COR Biosciences); anti-chicken IgY (H+L), 1:10,000 (Thermo Fisher Scientific)] and imaged on a LI-COR imager (Odyssey CLx).

Drosophila larval preparations and IHC

Third-instar larvae or adult *Drosophila* brains were dissected, fixed, and immunostained as previously described (*140*). Briefly, animals were dissected in ice-cold PBS (Lonza, #17-516F), fixed in 4% formaldehyde, washed three times in PBS, incubated in 5% Triton X-100/PBS for 20 min, washed three times in 0.1% PBST (0.1% Triton X-100/PBS), and incubated overnight with the primary antibody mouse anti–lamin Dm0 (1:200, Developmental Studies Hybridoma Bank). Larvae were washed three times in 0.1% PBST and incubated with secondary antibodies: anti-mouse Alexa Flour 647 (1:100, Invitrogen, #28181). Stained larvae were mounted using DAPI (4′,6-diamidino-2-phenylindole) Fluoroshield (Sigma-Aldrich, #F6182). Images were collected on a Nikon A1 eclipse T_i confocal microscope.

Quantitative image acquisition and analysis

Images used for quantification were acquired at matched exposure times or laser settings and processed using identical settings. Quantifications were normalized within each respective experiment with $n \geq 3$ independent experiments unless otherwise specified in figure legends. Image acquisition for HEK-293 experiments was performed on a Leica DMI4000B laser scanning confocal microscope (Leica, Buffalo Grove, IL) or with Leica DMi8 microscope (Leica, Buffalo Grove, IL) using a C10600-ORCA-R2 digital CCD (charge-coupled device) camera (Hamamatsu Photonics, Japan) and processed with Fiji. For high-resolution images and 3D reconstructions, Nikon W1 Dual CAM spinning disk and Imaris Cell Imaging software were used.

Quantitative live cell imaging and analysis of GFP- and GFP-$(GR)_{50}$–transduced iPSC-derived MNs were performed through an IncuCyte System (Sartorious). Tracking of neuronal survival was manually performed with Fiji. Longitudinal tracking of iMNs was performed with a Molecular Devices ImageExpress once every 48 hours. Neuronal survival was tracked using SVcell 3.0 (DRVision Technologies) or ImageJ. Neurons were scored as dead when their soma was no longer detectable by RFP fluorescence.

Experimental study design and statistical analysis

No statistical method was used to determine the sample size. We determined the size of the samples based on our experience with the used experimental models and the standards in the field. No data were excluded from the analysis. All biological experiments were replicated two or more times (biological replicates), initially analyzed independently, and subsequently combined for a final analysis. All samples were allocated based on their treatment condition. Blinding procedures were applied for image analysis; the operator that imaged and analyzed the samples was different from the operator that experimentally prepared the samples.

All statistical analyses were done with Prism 7 software (GraphPad Software), R 4.2.1 (*141*), and R packages lme4 and multicom (*142*, *143*). Individual values are displayed as dots in the graphs and represent all values measured in the study. The sample size (n) of each specific experiment is provided in Results, and the statistical test performed for each specific experiment is defined in the corresponding figure legend. For each statistical analysis, we first tested whether sample data fit into Gaussian distribution using the D′Agostino-Pearson omnibus normality test. To compare two experimental conditions, either a Student′s t test (parametric) or a Mann-Whitney U test (nonparametric) was performed. To compare three or more experimental conditions, one-way analysis of variance (ANOVA) followed by Tukey post hoc test (parametric) or Kruskal-Wallis rank test (nonparametric) was performed. To compare effects of treatment conditions in superplots, a statistical model for the response was considered, with fixed effects linked to treatments and with each individual experiment considered as randomized blocks. Analyzed parameters (response variable) were defined by logarithmic transformation over the original variable to guarantee the normal behavior of statistical model residuals (pure error). Then, multiple comparisons based on Tukey contrasts were performed to compare treatment effects (fixed effects) into the statistical model. For comparisons of survival curves in Kaplan-Meier plots, we used Gehan-Breslow-Wilcoxon test.

Supplementary Materials

This PDF file includes:
Figs. S1 to S10
Legends for tables S1 to S6

Other Supplementary Material for this manuscript includes the following:
Tables S1 to S6

REFERENCES AND NOTES

1. A. E. Renton, E. Majounie, A. Waite, J. Simon-Sanchez, S. Rollinson, J. R. Gibbs, J. C. Schymick, H. Laaksovirta, J. C. van Swieten, L. Myllykangas, H. Kalimo, A. Paetau, Y. Abramzon, A. M. Remes, A. Kaganovich, S. W. Scholz, J. Duckworth, J. Ding, D. W. Harmer, D. G. Hernandez, J. O. Johnson, K. Mok, M. Ryten, D. Trabzuni, R. J. Guerreiro, R. W. Orrell, J. Neal, A. Murray, J. Pearson, I. E. Jansen, D. Sondervan, H. Seelaar, D. Blake, K. Young, N. Halliwell, J. B. Callister, G. Toulson, A. Richardson, A. Gerhard, J. Snowden, D. Mann, D. Neary, M. A. Nalls, T. Peuralinna, L. Jansson, V. M. Isoviita, A. L. Kaivorinne, M. Holtta-Vuori, E. Ikonen, R. Sulkava, M. Benatar, J. Wuu, A. Chio, G. Restagno, G. Borghero, M. Sabatelli; ITALSGEN Consortium, D. Heckerman, E. Rogaeva, L. Zinman, J. D. Rothstein, M. Sendtner, C. Drepper, E. E. Eichler, C. Alkan, Z. Abdullaev, S. D. Pack, A. Dutra, E. Pak, J. Hardy, A. Singleton, N. M. Williams, P. Heutink, S. Pickering-Brown, H. R. Morris, P. J. Tienari, B. J. Traynor, A hexanucleotide repeat expansion in C9ORF72 is the cause of chromosome 9p21-linked ALS-FTD. *Neuron* **72**, 257–268 (2011).
2. M. DeJesus-Hernandez, I. R. Mackenzie, B. F. Boeve, A. L. Boxer, M. Baker, N. J. Rutherford, A. M. Nicholson, N. A. Finch, H. Flynn, J. Adamson, N. Kouri, A. Wojtas, P. Sengdy, G. Y. Hsiung, A. Karydas, W. W. Seeley, K. A. Josephs, G. Coppola, D. H. Geschwind, Z. K. Wszolek, H. Feldman, D. S. Knopman, R. C. Petersen, B. L. Miller, D. W. Dickson, K. B. Boylan, N. R. Graff-Radford, R. Rademakers, Expanded GGGGCC hexanucleotide repeat in noncoding region of C9ORF72 causes chromosome 9p-linked FTD and ALS. *Neuron* **72**, 245–256 (2011).

3. C. J. Donnelly, P. W. Zhang, J. T. Pham, A. R. Haeusler, N. A. Mistry, S. Vidensky, E. L. Daley, E. M. Poth, B. Hoover, D. M. Fines, N. Maragakis, P. J. Tienari, L. Petrucelli, B. J. Traynor, J. Wang, F. Rigo, C. F. Bennett, S. Blackshaw, R. Sattler, J. D. Rothstein, RNA toxicity from the ALS/FTD C9ORF72 expansion is mitigated by antisense intervention. *Neuron* **80**, 415–428 (2013).
4. K. Mori, T. Arzberger, F. A. Grasser, I. Gijselinck, S. May, K. Rentzsch, S. M. Weng, M. H. Schludi, J. van der Zee, M. Cruts, C. Van Broeckhoven, E. Kremmer, H. A. Kretzschmar, C. Haass, D. Edbauer, Bidirectional transcripts of the expanded C9orf72 hexanucleotide repeat are translated into aggregating dipeptide repeat proteins. *Acta Neuropathol.* **126**, 881–893 (2013).
5. P. E. Ash, K. F. Bieniek, T. F. Gendron, T. Caulfield, W. L. Lin, M. Dejesus-Hernandez, M. M. van Blitterswijk, K. Jansen-West, J. W. Paul 3rd, R. Rademakers, K. B. Boylan, D. W. Dickson, L. Petrucelli, Unconventional translation of C9ORF72 GGGGCC expansion generates insoluble polypeptides specific to c9FTD/ALS. *Neuron* **77**, 639–646 (2013).
6. T. Zu, Y. Liu, M. Banez-Coronel, T. Reid, O. Pletnikova, J. Lewis, T. M. Miller, M. B. Harms, A. E. Falchook, S. H. Subramony, L. W. Ostrow, J. D. Rothstein, J. C. Troncoso, L. P. W. Ranum, RAN proteins and RNA foci from antisense transcripts in C9ORF72 ALS and frontotemporal dementia. *Proc. Natl. Acad. Sci. U.S.A.* **110**, E4968–E4977 (2013).
7. B. D. Freibaum, J. P. Taylor, The role of dipeptide repeats in C9ORF72-related ALS-FTD. *Front. Mol. Neurosci.* **10**, 35 (2017).
8. R. Balendra, A. M. Isaacs, C9orf72-mediated ALS and FTD: Multiple pathways to disease. *Nat. Rev. Neurol.* **14**, 544–558 (2018).
9. A. R. Haeusler, C. J. Donnelly, J. D. Rothstein, The expanding biology of the C9orf72 nucleotide repeat expansion in neurodegenerative disease. *Nat. Rev. Neurosci.* **17**, 383–395 (2016).
10. B. D. Freibaum, Y. Lu, R. Lopez-Gonzalez, N. C. Kim, S. Almeida, K.-H. Lee, N. Badders, M. Valentine, B. L. Miller, P. C. Wong, L. Petrucelli, H. J. Kim, F.-B. Gao, J. P. Taylor, GGGGCC repeat expansion in C9orf72 compromises nucleocytoplasmic transport. *Nature* **525**, 129–133 (2015).
11. K.-H. Lee, P. Zhang, H. J. Kim, D. M. Mitrea, M. Sarkar, B. D. Freibaum, J. Cika, M. Coughlin, J. Messing, A. Molliex, B. A. Maxwell, N. C. Kim, J. Temirov, J. Moore, R.-M. Kolaitis, T. I. Shaw, B. Bai, J. Peng, R. W. Kriwacki, J. P. Taylor, C9orf72 dipeptide repeats impair the assembly, dynamics, and function of membrane-less organelles. *Cell* **167**, 774–788.e17 (2016).
12. S. Mizielinska, S. Gronke, T. Niccoli, C. E. Ridler, E. L. Clayton, A. Devoy, T. Moens, F. E. Norona, I. O. C. Woollacott, J. Pietrzyk, K. Cleverley, A. J. Nicoll, S. Pickering-Brown, J. Dols, M. Cabecinha, O. Hendrich, P. Fratta, E. M. C. Fisher, L. Partridge, A. M. Isaacs, C9orf72 repeat expansions cause neurodegeneration in Drosophila through arginine-rich proteins. *Science* **345**, 1192–1194 (2014).
13. S. Y. Choi, R. Lopez-Gonzalez, G. Krishnan, H. L. Phillips, A. N. Li, W. W. Seeley, W.-D. Yao, S. Almeida, F.-B. Gao, C9ORF72-ALS/FTD-associated poly(GR) binds Atp5a1 and compromises mitochondrial function in vivo. *Nat. Neurosci.* **22**, 851–862 (2019).
14. Z. Hao, L. Liu, Z. Tao, R. Wang, H. Ren, H. Sun, Z. Lin, Z. Zhang, C. Mu, J. Zhou, G. Wang, Motor dysfunction and neurodegeneration in a C9orf72 mouse line expressing poly-PR. *Nat. Commun.* **10**, 2906 (2019).
15. Z. Tao, H. Wang, Q. Xia, K. Li, K. Li, X. Jiang, G. Xu, G. Wang, Z. Ying, Nucleolar stress and impaired stress granule formation contribute to C9orf72 RAN translation-induced cytotoxicity. *Hum. Mol. Genet.* **24**, 2426–2441 (2015).
16. X. Wen, W. Tan, T. Westergard, K. Krishnamurthy, S. S. Markandaiah, Y. Shi, S. Lin, N. A. Shneider, J. Monaghan, U. B. Pandey, P. Pasinelli, J. K. Ichida, D. Trotti, Antisense proline-arginine RAN dipeptides linked to C9ORF72-ALS/FTD form toxic nuclear aggregates that initiate in vitro and in vivo neuronal death. *Neuron* **84**, 1213–1225 (2014).
17. Y.-J. Zhang, T. F. Gendron, M. T. W. Ebbert, A. D. O'Raw, M. Yue, K. Jansen-West, X. Zhang, M. Prudencio, J. Chew, C. N. Cook, L. M. Daughrity, J. Tong, Y. Song, S. R. Pickles, M. Castanedes-Casey, A. Kurti, R. Rademakers, B. Oskarsson, D. W. Dickson, W. Hu, A. D. Gitler, J. D. Fryer, L. Petrucelli, Poly(GR) impairs protein translation and stress granule dynamics in *C9orf72*-associated frontotemporal dementia and amyotrophic lateral sclerosis. *Nat. Med.* **24**, 1136–1142 (2018).
18. Y.-J. Zhang, L. Guo, P. K. Gonzales, T. F. Gendron, Y. Wu, K. Jansen-West, A. D. O'Raw, S. R. Pickles, M. Prudencio, Y. Carlomagno, M. A. Gachechiladze, C. Ludwig, R. Tian, J. Chew, M. DeTure, W. L. Lin, J. Tong, L. M. Daughrity, M. Yue, Y. Song, J. W. Andersen, M. Castanedes-Casey, A. Kurti, A. Datta, G. Antognetti, A. McCampbell, R. Rademakers, B. Oskarsson, D. W. Dickson, M. Kampmann, M. E. Ward, J. D. Fryer, C. D. Link, J. Shorter, L. Petrucelli, Heterochromatin anomalies and double-stranded RNA accumulation underlie *C9orf72* poly(PR) toxicity. *Science* **363**, eaav2606 (2019).
19. H. Hartmann, D. Hornburg, M. Czuppa, J. Bader, M. Michaelsen, D. Farny, T. Arzberger, M. Mann, F. Meissner, D. Edbauer, Proteomics and *C9orf72* neuropathology identify ribosomes as poly-GR/PR interactors driving toxicity. *Life Sci. Alliance* **1**, e201800070 (2018).
20. A. Jovicic, J. Mertens, S. Boeynaems, E. Bogaert, N. Chai, S. B. Yamada, J. W. Paul 3rd, S. Sun, J. R. Herdy, G. Bieri, N. J. Kramer, F. H. Gage, L. Van Den Bosch, W. Robberecht, A. D. Gitler, Modifiers of C9orf72 dipeptide repeat toxicity connect nucleocytoplasmic transport defects to FTD/ALS. *Nat. Neurosci.* **18**, 1226–1229 (2015).
21. K. Kanekura, T. Yagi, A. J. Cammack, J. Mahadevan, M. Kuroda, M. B. Harms, T. M. Miller, F. Urano, Poly-dipeptides encoded by the C9ORF72 repeats block global protein translation. *Hum. Mol. Genet.* **25**, 1803–1813 (2016).
22. I. Kwon, S. Xiang, M. Kato, L. Wu, P. Theodoropoulos, T. Wang, J. Kim, J. Yun, Y. Xie, S. L. McKnight, Poly-dipeptides encoded by the C9orf72 repeats bind nucleoli, impede RNA biogenesis, and kill cells. *Science* **345**, 1139–1145 (2014).
23. M. Radwan, C. S. Ang, A. R. Ormsby, D. Cox, J. C. Daly, G. E. Reid, D. M. Hatters, Arginine in *C9ORF72* dipolypeptides mediates promiscuous proteome binding and multiple modes of toxicity. *Mol. Cell. Proteomics* **19**, 640–654 (2020).
24. M. R. White, D. M. Mitrea, P. Zhang, C. B. Stanley, D. E. Cassidy, A. Nourse, A. H. Phillips, M. Tolbert, J. P. Taylor, R. W. Kriwacki, C9orf72 poly(PR) dipeptide repeats disturb biomolecular phase separation and disrupt nucleolar function. *Mol. Cell* **74**, 713–728 e6 (2019).
25. K. Zhang, J. G. Daigle, K. M. Cunningham, A. N. Coyne, K. Ruan, J. C. Grima, K. E. Bowen, H. Wadhwa, P. Yang, F. Rigo, J. P. Taylor, A. D. Gitler, J. D. Rothstein, T. E. Lloyd, Stress granule assembly disrupts nucleocytoplasmic transport. *Cell* **173**, 958–971.e17 (2018).
26. Y. Lin, E. Mori, M. Kato, S. Xiang, L. Wu, I. Kwon, S. L. McKnight, Toxic PR poly-dipeptides encoded by the C9orf72 repeat expansion target LC domain polymers. *Cell* **167**, 789–802.e12 (2016).
27. S. Yin, R. Lopez-Gonzalez, R. C. Kunz, J. Gangopadhyay, C. Borufka, S. P. Gygi, F. B. Gao, R. Reed, Evidence that C9ORF72 dipeptide repeat proteins associate with U2 snRNP to cause mis-splicing in ALS/FTD patients. *Cell Rep.* **19**, 2244–2256 (2017).
28. S. Boeynaems, E. Bogaert, D. Kovacs, A. Konijnenberg, E. Timmerman, A. Volkov, M. Guharoy, M. De Decker, T. Jaspers, V. H. Ryan, A. M. Janke, P. Baatsen, T. Vercruysse, R. M. Kolaitis, D. Daelemans, J. P. Taylor, N. Kedersha, P. Anderson, F. Impens, F. Sobott, J. Schymkowitz, F. Rousseau, N. L. Fawzi, W. Robberecht, P. Van Damme, P. Tompa, L. Van Den Bosch, Phase separation of C9orf72 dipeptide repeats perturbs stress granule dynamics. *Mol. Cell* **65**, 1044–1055 e5 (2017).
29. H. Jafarinia, E. van der Giessen, P. R. Onck, Phase separation of toxic dipeptide repeat proteins related to C9orf72 ALS/FTD. *Biophys. J.* **119**, 843–851 (2020).
30. A. Micsonai, F. Wien, L. Kernya, Y.-H. Lee, Y. Goto, M. Réfrégiers, J. Kardos, Accurate secondary structure prediction and fold recognition for circular dichroism spectroscopy. *Proc. Natl. Acad. Sci. U.S.A.* **112**, E3095–E3103 (2015).
31. A. Micsonai, F. Wien, É. Bulyáki, J. Kun, É. Moussong, Y.-H. Lee, Y. Goto, M. Réfrégiers, J. Kardos, BeStSel: A web server for accurate protein secondary structure prediction and fold recognition from the circular dichroism spectra. *Nucleic Acids Res.* **46**, W315–W322 (2018).
32. A. Barth, The infrared absorption of amino acid side chains. *Prog. Biophys. Mol. Biol.* **74**, 141–173 (2000).
33. A. Barth, C. Zscherp, What vibrations tell us about proteins. *Q. Rev. Biophys.* **35**, 369–430 (2002).
34. Y.-J. Chang, U.-S. Jeng, Y.-L. Chiang, I.-S. Hwang, Y.-R. Chen, The glycine-alanine dipeptide repeat from C9orf72 hexanucleotide expansions forms toxic amyloids possessing cell-to-cell transmission properties. *J. Biol. Chem.* **291**, 4903–4911 (2016).
35. I. R. Mackenzie, P. Frick, F. A. Grasser, T. F. Gendron, L. Petrucelli, N. R. Cashman, D. Edbauer, E. Kremmer, J. Prudlo, D. Troost, M. Neumann, Quantitative analysis and clinico-pathological correlations of different dipeptide repeat protein pathologies in C9ORF72 mutation carriers. *Acta Neuropathol.* **130**, 845–861 (2015).
36. J. Gomez-Deza, Y. B. Lee, C. Troakes, M. Nolan, S. Al-Sarraj, J. M. Gallo, C. E. Shaw, Dipeptide repeat protein inclusions are rare in the spinal cord and almost absent from motor neurons in C9ORF72 mutant amyotrophic lateral sclerosis and are unlikely to cause their degeneration. *Acta Neuropathol. Commun.* **3**, 38 (2015).
37. S. Saberi, J. E. Stauffer, J. Jiang, S. D. Garcia, A. E. Taylor, D. Schulte, T. Ohkubo, C. L. Schloffman, M. Maldonado, M. Baughn, M. J. Rodriguez, D. Pizzo, D. Cleveland, J. Ravits, Sense-encoded poly-GR dipeptide repeat proteins correlate to neurodegeneration and uniquely co-localize with TDP-43 in dendrites of repeat-expanded C9orf72 amyotrophic lateral sclerosis. *Acta Neuropathol.* **135**, 459–474 (2018).
38. J. C. Darnell, A. Mele, K. Y. S. Hung, R. B. Darnell, Immunoprecipitation and SDS-PAGE for cross-linking immunoprecipitation (CLIP). *Cold Spring Harb. Protoc.*, (2018).
39. T. A. Potapova, J. L. Gerton, Ribosomal DNA and the nucleolus in the context of genome organization. *Chromosome Res.* **27**, 109–127 (2019).
40. E. S. Lander, L. M. Linton, B. Birren, C. Nusbaum, M. C. Zody, J. Baldwin, K. Devon, K. Dewar, M. Doyle, W. FitzHugh, R. Funke, D. Gage, K. Harris, A. Heaford, J. Howland, L. Kann, J. Lehoczky, R. LeVine, P. McEwan, K. McKernan, J. Meldrim, J. P. Mesirov, C. Miranda, W. Morris, J. Naylor, C. Raymond, M. Rosetti, R. Santos, A. Sheridan, C. Sougnez, Y. Stange-Thomann, N. Stojanovic, A. Subramanian, D. Wyman, J. Rogers, J. Sulston, R. Ainscough, S. Beck, D. Bentley, J. Burton, C. Clee, N. Carter, A. Coulson, R. Deadman, P. Deloukas,

A. Dunham, I. Dunham, R. Durbin, L. French, D. Grafham, S. Gregory, T. Hubbard, S. Humphray, A. Hunt, M. Jones, C. Lloyd, A. McMurray, L. Matthews, S. Mercer, S. Milne, J. C. Mullikin, A. Mungall, R. Plumb, M. Ross, R. Shownkeen, S. Sims, R. H. Waterston, R. K. Wilson, L. W. Hillier, J. D. McPherson, M. A. Marra, E. R. Mardis, L. A. Fulton, A. T. Chinwalla, K. H. Pepin, W. R. Gish, S. L. Chissoe, M. C. Wendl, K. D. Delehaunty, T. L. Miner, A. Delehaunty, J. B. Kramer, L. L. Cook, R. S. Fulton, D. L. Johnson, P. J. Minx, S. W. Clifton, T. Hawkins, E. Branscomb, P. Predki, P. Richardson, S. Wenning, T. Slezak, N. Doggett, J. F. Cheng, A. Olsen, S. Lucas, C. Elkin, E. Uberbacher, M. Frazier, R. A. Gibbs, D. M. Muzny, S. E. Scherer, J. B. Bouck, E. J. Sodergren, K. C. Worley, C. M. Rives, J. H. Gorrell, M. L. Metzker, S. L. Naylor, R. S. Kucherlapati, D. L. Nelson, G. M. Weinstock, Y. Sakaki, A. Fujiyama, M. Hattori, T. Yada, A. Toyoda, T. Itoh, C. Kawagoe, H. Watanabe, Y. Totoki, T. Taylor, J. Weissenbach, R. Heilig, W. Saurin, F. Artiguenave, P. Brottier, T. Bruls, E. Pelletier, C. Robert, P. Wincker, D. R. Smith, L. Doucette-Stamm, M. Rubenfield, K. Weinstock, H. M. Lee, J. Dubois, A. Rosenthal, M. Platzer, G. Nyakatura, S. Taudien, A. Rump, H. Yang, J. Yu, J. Wang, G. Huang, J. Gu, L. Hood, L. Rowen, A. Madan, S. Qin, R. W. Davis, N. A. Federspiel, A. P. Abola, M. J. Proctor, R. M. Myers, J. Schmutz, M. Dickson, J. Grimwood, D. R. Cox, M. V. Olson, R. Kaul, C. Raymond, N. Shimizu, K. Kawasaki, S. Minoshima, G. A. Evans, M. Athanasiou, R. Schultz, B. A. Roe, F. Chen, H. Pan, J. Ramser, H. Lehrach, R. Reinhardt, W. R. McCombie, M. de la Bastide, N. Dedhia, H. Blocker, K. Hornischer, G. Nordsiek, R. Agarwala, L. Aravind, J. A. Bailey, A. Bateman, S. Batzoglou, E. Birney, P. Bork, D. G. Brown, C. B. Burge, L. Cerutti, H. C. Chen, D. Church, M. Clamp, R. R. Copley, T. Doerks, S. R. Eddy, E. E. Eichler, T. S. Furey, J. Galagan, J. G. Gilbert, C. Harmon, Y. Hayashizaki, D. Haussler, H. Hermjakob, K. Hokamp, W. Jang, L. S. Johnson, T. A. Jones, S. Kasif, A. Kaspryzk, S. Kennedy, W. J. Kent, P. Kitts, E. V. Koonin, I. Korf, D. Kulp, D. Lancet, T. M. Lowe, A. McLysaght, T. Mikkelsen, J. V. Moran, N. Mulder, V. J. Pollara, C. P. Ponting, G. Schuler, J. Schultz, G. Slater, A. F. Smit, E. Stupka, J. Szustakowki, D. Thierry-Mieg, J. Thierry-Mieg, L. Wagner, J. Wallis, R. Wheeler, A. Williams, Y. I. Wolf, K. H. Wolfe, S. P. Yang, R. F. Yeh, F. Collins, M. S. Guyer, J. Peterson, A. Felsenfeld, K. A. Wetterstrand, A. Patrinos, M. J. Morgan, P. de Jong, J. J. Catanese, K. Osoegawa, H. Shizuya, S. Choi, Y. J. Chen, J. Szustakowki; International Human Genome Sequencing Consortium, Initial sequencing and analysis of the human genome. *Nature* **409**, 860–921 (2001).

41. I. Huppertz, J. Attig, A. D'Ambrogio, L. E. Easton, C. R. Sibley, Y. Sugimoto, M. Tajnik, J. König, J. Ule, iCLIP: Protein-RNA interactions at nucleotide resolution. *Methods* **65**, 274–287 (2014).
42. M. Preti, M.-F. O'Donohue, N. Montel-Lehry, M.-L. Bortolin-Cavaillé, V. Choesmel, P.-E. Gleizes, Gradual processing of the ITS1 from the nucleolus to the cytoplasm during synthesis of the human 18S rRNA. *Nucleic Acids Res.* **41**, 4709–4723 (2013).
43. A. B. Loveland, E. Svidritskiy, D. Susorov, S. Lee, A. Park, S. Zvornicanin, G. Demo, F. B. Gao, A. A. Korostelev, Ribosome inhibition by C9ORF72-ALS/FTD-associated poly-PR and poly-GR proteins revealed by cryo-EM. *Nat. Commun.* **13**, 2776 (2022).
44. R. Lopez-Gonzalez, Y. Lu, T. F. Gendron, A. Karydas, H. Tran, D. Yang, L. Petrucelli, B. L. Miller, S. Almeida, F.-B. Gao, Poly(GR) in C9ORF72-related ALS/FTD compromises mitochondrial function and increases oxidative stress and DNA damage in iPSC-derived motor neurons. *Neuron* **92**, 383–391 (2016).
45. S. Shao, J. Murray, A. Brown, J. Taunton, V. Ramakrishnan, R. S. Hegde, Decoding mammalian ribosome-mRNA states by translational GTPase complexes. *Cell* **167**, 1229–1240 e15 (2016).
46. J. Sund, C. Lind, J. Åqvist, Binding site preorganization and ligand discrimination in the purine riboswitch. *J. Phys. Chem. B* **119**, 773–782 (2015).
47. R. P. Bahadur, S. Kannan, M. Zacharias, Binding of the bacteriophage P22 N-peptide to the boxB RNA motif studied by molecular dynamics simulations. *Biophys. J.* **97**, 3139–3149 (2009).
48. M. J. Ziller, J. A. Ortega, K. A. Quinlan, D. P. Santos, H. Gu, E. J. Martin, C. Galonska, R. Pop, S. Maidl, A. Di Pardo, M. Huang, H. Y. Meltzer, A. Gnirke, C. J. Heckman, A. Meissner, E. Kiskinis, Dissecting the functional consequences of de novo DNA methylation dynamics in human motor neuron differentiation and physiology. *Cell Stem Cell* **22**, 559–574.e9 (2018).
49. Y. Shi, S. Lin, K. A. Staats, Y. Li, W. H. Chang, S. T. Hung, E. Hendricks, G. R. Linares, Y. Wang, E. Y. Son, X. Wen, K. Kisler, B. Wilkinson, L. Menendez, T. Sugawara, P. Woolwine, M. Huang, M. J. Cowan, B. Ge, N. Koutsodendris, K. P. Sandor, J. Komberg, V. R. Vangoor, K. Senthilkumar, V. Hennes, C. Seah, A. R. Nelson, T. Y. Cheng, S. J. Lee, P. R. August, J. A. Chen, N. Wisniewski, V. Hanson-Smith, T. G. Belgard, A. Zhang, M. Coba, C. Grunseich, M. E. Ward, L. H. van den Berg, R. J. Pasterkamp, D. Trotti, B. V. Zlokovic, J. K. Ichida, Haploinsufficiency leads to neurodegeneration in *C9ORF72* ALS/FTD human induced motor neurons. *Nat. Med.* **24**, 313–325 (2018).
50. S.-T. Hung, G. R. Linares, W.-H. Chang, Y. Eoh, G. Krishnan, S. Mendonca, S. Hong, Y. Shi, M. Santana, C. Kueth, S. Macklin-Isquierdo, S. Perry, S. Duhaime, C. Maios, J. Chang, J. Perez, A. Couto, J. Lai, Y. Li, S. V. Alworth, E. Hendricks, Y. Wang, B. V. Zlokovic, D. K. Dickman, J. A. Parker, D. C. Zarnescu, F.-B. Gao, J. K. Ichida, PIKFYVE inhibition mitigates disease in models of diverse forms of ALS. *Cell* **186**, 786–802.e28 (2023).
51. L. R. Muenz, S. B. Green, D. P. Byar, Applications of the Mantel-Haenszel statistic to the comparison of survival distributions. *Biometrics* **33**, 617–626 (1977).
52. S. Zheng, A. Sahimi, K. S. Shing, M. Sahimi, Molecular dynamics study of structure, folding, and aggregation of poly-PR and poly-GR proteins. *Biophys. J.* **120**, 64–72 (2021).
53. K. Kanekura, Y. Harada, M. Fujimoto, T. Yagi, Y. Hayamizu, K. Nagaoka, M. Kuroda, Characterization of membrane penetration and cytotoxicity of C9orf72-encoding arginine-rich dipeptides. *Sci. Rep.* **8**, 12740 (2018).
54. B. N. Flores, M. E. Dulchavsky, A. Krans, M. R. Sawaya, H. L. Paulson, P. K. Todd, S. J. Barmada, M. I. Ivanova, Distinct C9orf72-associated dipeptide repeat structures correlate with neuronal toxicity. *PLOS ONE* **11**, e0165084 (2016).
55. P. Cossio, A. Trovato, F. Pietrucci, F. Seno, A. Maritan, A. Laio, Exploring the universe of protein structures beyond the Protein Data Bank. *PLOS Comput. Biol.* **6**, e1000957 (2010).
56. S. Zamuner, A. Rodriguez, F. Seno, A. Trovato, An efficient algorithm to perform local concerted movements of a chain molecule. *PLOS ONE* **10**, e0118342 (2015).
57. C. Cardelli, F. Nerattini, L. Tubiana, V. Bianco, C. Dellago, F. Sciortino, I. Coluzza, General methodology to identify the minimum alphabet size for heteropolymer design. *Adv. Theory Simul.* **2**, 1900031 (2019).
58. F. Nerattini, L. Tubiana, C. Cardelli, V. Bianco, C. Dellago, I. Coluzza, Protein design under competing conditions for the availability of amino acids. *Sci. Rep.* **10**, 2684 (2020).
59. I. Gijselinck, S. Van Mossevelde, J. van der Zee, A. Sieben, S. Engelborghs, J. De Bleecker, A. Ivanoiu, O. Deryck, D. Edbauer, M. Zhang, B. Heeman, V. Bäumer, M. Van den Broeck, M. Mattheijssens, K. Peeters, E. Rogaeva, P. De Jonghe, P. Cras, J. J. Martin, P. P. de Deyn, M. Cruts, C. Van Broeckhoven; on behalf of the BELNEU CONSORTIUM, The C9orf72 repeat size correlates with onset age of disease, DNA methylation and transcriptional downregulation of the promoter. *Mol. Psychiatry* **21**, 1112–1124 (2016).
60. T. F. Gendron, J. Chew, J. N. Stankowski, L. R. Hayes, Y. J. Zhang, M. Prudencio, Y. Carlomagno, L. M. Daughrity, K. Jansen-West, E. A. Perkerson, A. O'Raw, C. Cook, L. Pregent, V. Belzil, M. van Blitterswijk, L. J. Tabassian, C. W. Lee, M. Yue, J. Tong, Y. Song, M. Castanedes-Casey, L. Rousseau, V. Phillips, D. W. Dickson, R. Rademakers, J. D. Fryer, B. K. Rush, O. Pedraza, A. M. Caputo, P. Desaro, C. Palmucci, A. Robertson, M. G. Heckman, N. N. Diehl, E. Wiggs, M. Tierney, L. Braun, J. Farren, D. Lacomis, S. Ladha, C. N. Fournier, L. F. McCluskey, L. B. Elman, J. B. Toledo, J. D. McBride, C. Tiloca, C. Morelli, B. Poletti, F. Solca, A. Prelle, J. Wuu, J. Jockel-Balsarotti, F. Rigo, C. Ambrose, A. Datta, W. Yang, D. Raitcheva, G. Antognetti, A. McCampbell, J. C. Van Swieten, B. L. Miller, A. L. Boxer, R. H. Brown, R. Bowser, T. M. Miller, J. Q. Trojanowski, M. Grossman, J. D. Berry, W. T. Hu, A. Ratti, B. J. Traynor, M. D. Disney, M. Benatar, V. Silani, J. D. Glass, M. K. Floeter, J. D. Rothstein, K. B. Boylan, L. Petrucelli, Poly(GP) proteins are a useful pharmacodynamic marker for *C9ORF72*-associated amyotrophic lateral sclerosis. *Sci. Transl. Med.* **9**, eaai7866 (2017).
61. A. J. Cammack, N. Atassi, T. Hyman, L. H. van den Berg, M. Harms, R. H. Baloh, R. H. Brown, M. A. van Es, J. H. Veldink, B. S. de Vries, J. D. Rothstein, C. Drain, J. Jockel-Balsarotti, A. Malcolm, S. Boodram, A. Salter, N. Wightman, H. Yu, A. V. Sherman, T. J. Esparza, D. McKenna-Yasek, M. A. Owegi, C. Douthwright, A. McCampbell, T. Ferguson, C. Cruchaga, M. Cudkowicz, T. M. Miller, Prospective natural history study of *C9orf72* ALS clinical characteristics and biomarkers. *Neurology* **93**, e1605–e1617 (2019).
62. M. van Blitterswijk, M. DeJesus-Hernandez, E. Niemantsverdriet, M. E. Murray, M. G. Heckman, N. N. Diehl, P. H. Brown, M. C. Baker, N. A. Finch, P. O. Bauer, G. Serrano, T. G. Beach, K. A. Josephs, D. S. Knopman, R. C. Petersen, B. F. Boeve, N. R. Graff-Radford, K. B. Boylan, L. Petrucelli, D. W. Dickson, R. Rademakers, Association between repeat sizes and clinical and pathological characteristics in carriers of C9ORF72 repeat expansions (Xpansize-72): A cross-sectional cohort study. *Lancet Neurol.* **12**, 978–988 (2013).
63. E. Suh, E. B. Lee, D. Neal, E. M. Wood, J. B. Toledo, L. Rennert, D. J. Irwin, C. T. McMillan, B. Krock, L. B. Elman, L. F. McCluskey, M. Grossman, S. X. Xie, J. Q. Trojanowski, V. M. Van Deerlin, Semi-automated quantification of C9orf72 expansion size reveals inverse correlation between hexanucleotide repeat number and disease duration in frontotemporal degeneration. *Acta Neuropathol.* **130**, 363–372 (2015).
64. R. Tabet, L. Schaeffer, F. Freyermuth, M. Jambeau, M. Workman, C. Z. Lee, C. C. Lin, J. Jiang, K. Jansen-West, H. Abou-Hamdan, L. Désaubry, T. Gendron, L. Petrucelli, F. Martin, C. Lagier-Tourenne, CUG initiation and frameshifting enable production of dipeptide repeat proteins from ALS/FTD C9ORF72 transcripts. *Nat. Commun.* **9**, 152 (2018).
65. Z. T. McEachin, J. Parameswaran, N. Raj, G. J. Bassell, J. Jiang, RNA-mediated toxicity in C9orf72 ALS and FTD. *Neurobiol. Dis.* **145**, 105055 (2020).
66. J. Bennion Callister, S. Ryan, J. Sim, S. Rollinson, S. M. Pickering-Brown, Modelling C9orf72 dipeptide repeat proteins of a physiologically relevant size. *Hum. Mol. Genet.* **25**, 5069–5082 (2016).
67. T. G. Moens, T. Niccoli, K. M. Wilson, M. L. Atilano, N. Birsa, L. M. Gittings, B. V. Holbling, M. C. Dyson, A. Thoeng, J. Neeves, I. Glaria, L. Yu, J. Bussmann, E. Storkebaum, M. Pardo, J. S. Choudhary, P. Fratta, L. Partridge, A. M. Isaacs, C9orf72 arginine-rich dipeptide proteins interact with ribosomal proteins in vivo to induce a toxic translational arrest that is rescued by eIF1A. *Acta Neuropathol.* **137**, 487–500 (2019).

68. E. M. Tank, C. Figueroa-Romero, L. M. Hinder, K. Bedi, H. C. Archbold, X. Li, K. Weskamp, N. Safren, X. Paez-Colasante, C. Pacut, S. Thumma, M. T. Paulsen, K. Guo, J. Hur, M. Ljungman, E. L. Feldman, S. J. Barmada, Abnormal RNA stability in amyotrophic lateral sclerosis. *Nat. Commun.* **9**, 2845 (2018).
69. K. Y. Shi, E. Mori, Z. F. Nizami, Y. Lin, M. Kato, S. Xiang, L. C. Wu, M. Ding, Y. Yu, J. G. Gall, S. L. McKnight, Toxic PR_n poly-dipeptides encoded by the *C9orf72* repeat expansion block nuclear import and export. *Proc. Natl. Acad. Sci. U.S.A.* **114**, E1111–E1117 (2017).
70. J. Vanneste, T. Vercruysse, S. Boeynaems, A. Sicart, P. Van Damme, D. Daelemans, L. Van Den Bosch, C9orf72-generated poly-GR and poly-PR do not directly interfere with nucleocytoplasmic transport. *Sci. Rep.* **9**, 15728 (2019).
71. L. R. Hayes, L. Duan, K. Bowen, P. Kalab, J. D. Rothstein, *C9orf72* arginine-rich dipeptide repeat proteins disrupt karyopherin-mediated nuclear import. *eLife* **9**, e51685 (2020).
72. S. Boeynaems, A. S. Holehouse, V. Weinhardt, D. Kovacs, J. Van Lindt, C. Larabell, L. Van Den Bosch, R. Das, P. S. Tompa, R. V. Pappu, A. D. Gitler, Spontaneous driving forces give rise to protein-RNA condensates with coexisting phases and complex material properties. *Proc. Natl. Acad. Sci. U.S.A.* **116**, 7889–7898 (2019).
73. V. Lafarga, O. Sirozh, I. Díaz-López, A. Galarreta, M. Hisaoka, E. Zarzuela, J. Boskovic, B. Jovanovic, R. Fernandez-Leiro, J. Muñoz, G. Stoecklin, I. Ventoso, O. Fernandez-Capetillo, Widespread displacement of DNA- and RNA-binding factors underlies toxicity of arginine-rich cell-penetrating peptides. *EMBO J.* **40**, e103311 (2021).
74. V. N. Uversky, Disorder in the lifetime of a protein. *Intrinsically Disord. Proteins* **1**, e26782 (2013).
75. W. Xu, P. Bao, X. Jiang, H. Wang, M. Qin, R. Wang, T. Wang, Y. Yang, I. Lorenzini, L. Liao, R. Sattler, J. Xu, Reactivation of nonsense-mediated mRNA decay protects against *C9orf72* dipeptide-repeat neurotoxicity. *Brain* **142**, 1349–1364 (2019).
76. J. A. Ortega, E. L. Daley, S. Kour, M. Samani, L. Tellez, H. S. Smith, E. A. Hall, Y. T. Esengul, Y. H. Tsai, T. F. Gendron, C. J. Donnelly, T. Siddique, J. N. Savas, U. B. Pandey, E. Kiskinis, Nucleocytoplasmic proteomic analysis uncovers eRF1 and nonsense-mediated decay as modifiers of ALS/FTD *C9orf72* toxicity. *Neuron* **106**, 90–107.e13 (2020).
77. Y. Sun, A. Eshov, J. Zhou, A. U. Isiktas, J. U. Guo, C9orf72 arginine-rich dipeptide repeats inhibit UPF1-mediated RNA decay via translational repression. *Nat. Commun.* **11**, 3354 (2020).
78. R. Balendra, I. R. de Los Mozos, H. M. Odeh, I. Glaria, C. Milioto, K. M. Wilson, A. M. Ule, M. Hallegger, L. Masino, S. Martin, R. Patani, J. Shorter, J. Ule, A. M. Isaacs, Transcriptome-wide RNA binding analysis of C9orf72 poly(PR) dipeptides. *Life Sci. Alliance* **6**, e202201824 (2023).
79. H. Deng, V. A. Bloomfield, J. M. Benevides, G. J. Thomas Jr., Structural basis of polyamine-DNA recognition: Spermidine and spermine interactions with genomic B-DNAs of different GC content probed by Raman spectroscopy. *Nucleic Acids Res.* **28**, 3379–3385 (2000).
80. T. Antony, T. Thomas, A. Shirahata, T. J. Thomas, Selectivity of polyamines on the stability of RNA−DNA hybrids containing phosphodiester and phosphorothioate oligodeoxyribonucleotides. *Biochemistry* **38**, 10775–10784 (1999).
81. A. Kabir, G. Suresh Kumar, Binding of the biogenic polyamines to deoxyribonucleic acids of varying base composition: Base specificity and the associated energetics of the interaction. *PLOS ONE* **8**, e70510 (2013).
82. W. Cheng, S. Wang, A. A. Mestre, C. Fu, A. Makarem, F. Xian, L. R. Hayes, R. Lopez-Gonzalez, K. Drenner, J. Jiang, D. W. Cleveland, S. Sun, C9ORF72 GGGGCC repeat-associated non-AUG translation is upregulated by stress through eIF2α phosphorylation. *Nat. Commun.* **9**, 51 (2018).
83. Y. Sonobe, G. Ghadge, K. Masaki, A. Sendoel, E. Fuchs, R. P. Roos, Translation of dipeptide repeat proteins from the C9ORF72 expanded repeat is associated with cellular stress. *Neurobiol. Dis.* **116**, 155–165 (2018).
84. K. M. Green, M. R. Glineburg, M. G. Kearse, B. N. Flores, A. E. Linsalata, S. J. Fedak, A. C. Goldstrohm, S. J. Barmada, P. K. Todd, RAN translation at *C9orf72*-associated repeat expansions is selectively enhanced by the integrated stress response. *Nat. Commun.* **8**, 2005 (2017).
85. T. Westergard, K. McAvoy, K. Russell, X. Wen, Y. Pang, B. Morris, P. Pasinelli, D. Trotti, A. Haeusler, Repeat-associated non-AUG translation in C9orf72-ALS/FTD is driven by neuronal excitation and stress. *EMBO Mol. Med.* **11**, e9423 (2019).
86. S. B. Yamada, T. F. Gendron, T. Niccoli, N. R. Genuth, R. Grosely, Y. Shi, I. Glaria, N. J. Kramer, L. Nakayama, S. Fang, T. J. I. Dinger, A. Thoeng, G. Rocha, M. Barna, J. D. Puglisi, L. Partridge, J. K. Ichida, A. M. Isaacs, L. Petrucelli, A. D. Gitler, RPS25 is required for efficient RAN translation of C9orf72 and other neurodegenerative disease-associated nucleotide repeats. *Nat. Neurosci.* **22**, 1383–1388 (2019).
87. W. Cheng, S. Wang, Z. Zhang, D. W. Morgens, L. R. Hayes, S. Lee, B. Portz, Y. Xie, B. V. Nguyen, M. S. Haney, S. Yan, D. Dong, A. N. Coyne, J. Yang, F. Xian, D. W. Cleveland, Z. Qiu, J. D. Rothstein, J. Shorter, F.-B. Gao, M. C. Bassik, S. Sun, CRISPR-Cas9 screens identify the RNA helicase DDX3X as a repressor of C9ORF72 (GGGGCC)n repeat-associated non-AUG translation. *Neuron* **104**, 885–898.e8 (2019).
88. L. Nguyen, F. Montrasio, A. Pattamatta, S. K. Tusi, O. Bardhi, K. D. Meyer, L. Hayes, K. Nakamura, M. Banez-Coronel, A. Coyne, S. Guo, L. A. Laboissonniere, Y. Gu, S. Narayanan, B. Smith, R. M. Nitsch, M. W. Kankel, M. Rushe, J. Rothstein, T. Zu, J. Grimm, L. P. W. Ranum, Antibody therapy targeting RAN proteins rescues C9 ALS/FTD phenotypes in C9orf72 mouse model. *Neuron* **105**, 645–662.e11 (2020).
89. Q. Zhou, C. Lehmer, M. Michaelsen, K. Mori, D. Alterauge, D. Baumjohann, M. H. Schludi, J. Greiling, D. Farny, A. Flatley, R. Feederle, S. May, F. Schreiber, T. Arzberger, C. Kuhm, T. Klopstock, A. Hermann, C. Haass, D. Edbauer, Antibodies inhibit transmission and aggregation of *C9orf72* poly-GA dipeptide repeat proteins. *EMBO Mol. Med.* **9**, 687–702 (2017).
90. J. R. Mann, A. M. Gleixner, J. C. Mauna, E. Gomes, M. R. DeChellis-Marks, P. G. Needham, K. E. Copley, B. Hurtle, B. Portz, N. J. Pyles, L. Guo, C. B. Calder, Z. P. Wills, U. B. Pandey, J. K. Kofler, J. L. Brodsky, A. Thathiah, J. Shorter, C. J. Donnelly, RNA binding antagonizes neurotoxic phase transitions of TDP-43. *Neuron* **102**, 321–338 e8 (2019).
91. M. Jazurek, A. Ciesiolka, J. Starega-Roslan, K. Bilinska, W. J. Krzyzosiak, Identifying proteins that bind to specific RNAs—Focus on simple repeat expansion diseases. *Nucleic Acids Res.* **44**, 9050–9070 (2016).
92. H. M. Odeh, J. Shorter, Arginine-rich dipeptide-repeat proteins as phase disruptors in C9-ALS/FTD. *Emerg. Top Life Sci.* **4**, 293–305 (2020).
93. M. D. Hanwell, D. E. Curtis, D. C. Lonie, T. Vandermeersch, E. Zurek, G. R. Hutchison, Avogadro: An advanced semantic chemical editor, visualization, and analysis platform. *J. Chem.* **4**, 17 (2012).
94. M. Zuker, Mfold web server for nucleic acid folding and hybridization prediction. *Nucleic Acids Res.* **31**, 3406–3415 (2003).
95. M. Biesiada, K. Pachulska-Wieczorek, R. W. Adamiak, K. J. Purzycka, RNAComposer and RNA 3D structure prediction for nanotechnology. *Methods* **103**, 120–127 (2016).
96. M. J. Abraham, T. Murtola, R. Schulz, S. Páll, J. C. Smith, B. Hess, E. Lindahl, GROMACS: High performance molecular simulations through multi-level parallelism from laptops to supercomputers. *SoftwareX* **1–2**, 19–25 (2015).
97. B. R. Brooks, C. L. Brooks III, A. D. Mackerell Jr., L. Nilsson, R. J. Petrella, B. Roux, Y. Won, G. Archontis, C. Bartels, S. Boresch, A. Caflisch, L. Caves, Q. Cui, A. R. Dinner, M. Feig, S. Fischer, J. Gao, M. Hodoscek, W. Im, K. Kuczera, T. Lazaridis, J. Ma, V. Ovchinnikov, E. Paci, R. W. Pastor, C. B. Post, J. Z. Pu, M. Schaefer, B. Tidor, R. M. Venable, H. L. Woodcock, X. Wu, W. Yang, D. M. York, M. Karplus, CHARMM: The biomolecular simulation program. *J. Comput. Chem.* **30**, 1545–1614 (2009).
98. K. Vanommeslaeghe, E. Hatcher, C. Acharya, S. Kundu, S. Zhong, J. Shim, E. Darian, O. Guvench, P. Lopes, I. Vorobyov, A. D. Mackerell Jr., CHARMM general force field: A force field for drug-like molecules compatible with the CHARMM all-atom additive biological force fields. *J. Comput. Chem.* **31**, 671–690 (2010).
99. A. D. MacKerell, D. Bashford, M. Bellott, R. L. Dunbrack, J. D. Evanseck, M. J. Field, S. Fischer, J. Gao, H. Guo, S. Ha, D. Joseph-McCarthy, L. Kuchnir, K. Kuczera, F. T. K. Lau, C. Mattos, S. Michnick, T. Ngo, D. T. Nguyen, B. Prodhom, W. E. Reiher, B. Roux, M. Schlenkrich, J. C. Smith, R. Stote, J. Straub, M. Watanabe, J. Wiórkiewicz-Kuczera, D. Yin, M. Karplus, All-atom empirical potential for molecular modeling and dynamics studies of proteins. *J. Phys. Chem. B* **102**, 3586–3616 (1998).
100. A. D. MacKerell Jr., N. Banavali, N. Foloppe, Development and current status of the CHARMM force field for nucleic acids. *Biopolymers* **56**, 257–265 (2000).
101. R. B. Best, X. Zhu, J. Shim, P. E. M. Lopes, J. Mittal, M. Feig, A. D. MacKerell, Optimization of the additive CHARMM all-atom protein force field targeting improved sampling of the backbone ϕ, ψ and side-chain χ(1) and χ(2) dihedral angles. *J. Chem. Theory Comput.* **8**, 3257–3273 (2012).
102. E. J. Denning, U. D. Priyakumar, L. Nilsson, A. D. Mackerell Jr., Impact of 2′-hydroxyl sampling on the conformational properties of RNA: Update of the CHARMM all-atom additive force field for RNA. *J. Comput. Chem.* **32**, 1929–1943 (2011).
103. X. Zhu, P. E. M. Lopes, A. D. MacKerell Jr., Recent developments and applications of the CHARMM force fields. *Wiley Interdiscip. Rev. Comput. Mol. Sci.* **2**, 167–185 (2012).
104. N. J. Cook, W. Li, D. Berta, M. Badaoui, A. Ballandras-Colas, A. Nans, A. Kotecha, E. Rosta, A. N. Engelman, P. Cherepanov, Structural basis of second-generation HIV integrase inhibitor action and viral resistance. *Science* **367**, 806–810 (2020).
105. C.-M. Suomivuori, N. R. Latorraca, L. M. Wingler, S. Eismann, M. C. King, A. L. W. Kleinhenz, M. A. Skiba, D. P. Staus, A. C. Kruse, R. J. Lefkowitz, R. O. Dror, Molecular mechanism of biased signaling in a prototypical G protein–coupled receptor. *Science* **367**, 881–887 (2020).
106. A. A. Kognole, A. D. MacKerell, Mg^{2+} impacts the twister ribozyme through push-pull stabilization of nonsequential phosphate pairs. *Biophys. J.* **118**, 1424–1437 (2020).
107. A. Babaian, K. Rothe, D. Girodat, I. Minia, S. Djondovic, M. Milek, S. E. Spencer Miko, H. J. Wieden, M. Landthaler, G. B. Morin, D. L. Mager, Loss of m(1)acp^{3}Ψ ribosomal RNA modification is a major feature of cancer. *Cell Rep.* **31**, 107611 (2020).

108. W. L. Jorgensen, J. Chandrasekhar, J. D. Madura, R. W. Impey, M. L. Klein, Comparison of simple potential functions for simulating liquid water. *J. Chem. Phys.* **79**, 926–935 (1983).
109. W. Humphrey, A. Dalke, K. Schulten, VMD: Visual molecular dynamics. *J. Mol. Graph.* **14**, 33–38 (1996).
110. L. Verlet, Computer "experiments" on classical fluids. I. Thermodynamical properties of Lennard-Jones molecules. *Phys. Rev.* **159**, 98–103 (1967).
111. T. Darden, D. York, L. Pedersen, Particle mesh Ewald: An *N*·log(*N*) method for Ewald sums in large systems. *J. Chem. Phys.* **98**, 10089–10092 (1993).
112. G. Bussi, D. Donadio, M. Parrinello, Canonical sampling through velocity rescaling. *J. Chem. Phys.* **126**, 014101 (2007).
113. H. J. C. Berendsen, J. P. M. Postma, W. F. V. Gunsteren, A. DiNola, J. R. Haak, Molecular dynamics with coupling to an external bath. *J. Chem. Phys.* **81**, 3684–3690 (1984).
114. M. Parrinello, A. Rahman, Polymorphic transitions in single crystals: A new molecular dynamics method. *J. Appl. Phys.* **52**, 7182–7190 (1981).
115. S. J. Marrink, H. J. Risselada, S. Yefimov, D. P. Tieleman, A. H. de Vries, The MARTINI force field: Coarse grained model for biomolecular simulations. *J. Phys. Chem. B* **111**, 7812–7824 (2007).
116. L. Monticelli, S. K. Kandasamy, X. Periole, R. G. Larson, D. P. Tieleman, S.-J. Marrink, The MARTINI coarse-grained force field: Extension to proteins. *J. Chem. Theory Comput.* **4**, 819–834 (2008).
117. D. H. de Jong, G. Singh, W. F. D. Bennett, C. Arnarez, T. A. Wassenaar, L. V. Schäfer, X. Periole, D. P. Tieleman, S. J. Marrink, Improved parameters for the Martini coarse-grained protein force field. *J. Chem. Theory Comput.* **9**, 687–697 (2013).
118. P. W. Frederix, G. G. Scott, Y. M. Abul-Haija, D. Kalafatovic, C. G. Pappas, N. Javid, N. T. Hunt, R. V. Ulijn, T. Tuttle, Exploring the sequence space for (tri-)peptide self-assembly to design and discover new hydrogels. *Nat. Chem.* **7**, 30–37 (2015).
119. P. W. J. M. Frederix, R. V. Ulijn, N. T. Hunt, T. Tuttle, Virtual screening for dipeptide aggregation: Toward predictive tools for peptide self-assembly. *J. Phys. Chem. Lett.* **2**, 2380–2384 (2011).
120. D. H. de Jong, S. Baoukina, H. I. Ingólfsson, S. J. Marrink, Martini straight: Boosting performance using a shorter cutoff and GPUs. *Computer Phys. Commun.* **199**, 1–7 (2016).
121. H. Yang, S. Yang, J. Kong, A. Dong, S. Yu, Obtaining information about protein secondary structures in aqueous solution using Fourier transform IR spectroscopy. *Nat. Protoc.* **10**, 382–396 (2015).
122. G. L. Boulting, E. Kiskinis, G. F. Croft, M. W. Amoroso, D. H. Oakley, B. J. Wainger, D. J. Williams, D. J. Kahler, M. Yamaki, L. Davidow, C. T. Rodolfa, J. T. Dimos, S. Mikkilineni, A. B. MacDermott, C. J. Woolf, C. E. Henderson, H. Wichterle, K. Eggan, A functionally characterized test set of human induced pluripotent stem cells. *Nat. Biotechnol.* **29**, 279–286 (2011).
123. K. Okita, Y. Matsumura, Y. Sato, A. Okada, A. Morizane, S. Okamoto, H. Hong, M. Nakagawa, K. Tanabe, K.-i. Tezuka, T. Shibata, T. Kunisada, M. Takahashi, J. Takahashi, H. Saji, S. Yamanaka, A more efficient method to generate integration-free human iPS cells. *Nat. Methods* **8**, 409–412 (2011).
124. Y. Shi, S. T. Hung, G. Rocha, S. Lin, G. R. Linares, K. A. Staats, C. Seah, Y. Wang, M. Chickering, J. Lai, T. Sugawara, A. P. Sagare, B. V. Zlokovic, J. K. Ichida, Identification and therapeutic rescue of autophagosome and glutamate receptor defects in C9ORF72 and sporadic ALS neurons. *JCI Insight* **5**, e127736 (2019).
125. Y. J. Zhang, K. Jansen-West, Y. F. Xu, T. F. Gendron, K. F. Bieniek, W. L. Lin, H. Sasaguri, T. Caulfield, J. Hubbard, L. Daughrity, J. Chew, V. V. Belzil, M. Prudencio, J. N. Stankowski, M. Castanedes-Casey, E. Whitelaw, P. E. Ash, M. DeTure, R. Rademakers, K. B. Boylan, D. W. Dickson, L. Petrucelli, Aggregation-prone c9FTD/ALS poly(GA) RAN-translated proteins cause neurotoxicity by inducing ER stress. *Acta Neuropathol.* **128**, 505–524 (2014).
126. S. W. Wingett, S. Andrews, FastQ Screen: A tool for multi-genome mapping and quality control. *F1000Res.* **7**, 1338 (2018).
127. H. Li, B. Handsaker, A. Wysoker, T. Fennell, J. Ruan, N. Homer, G. Marth, G. Abecasis, R. Durbin; 1000 Genome Project Data Processing Subgroup, The sequence alignment/map format and SAMtools. *Bioinformatics* **25**, 2078–2079 (2009).
128. T. Smith, A. Heger, I. Sudbery, UMI-tools: Modeling sequencing errors in unique molecular identifiers to improve quantification accuracy. *Genome Res.* **27**, 491–499 (2017).
129. A. R. Quinlan, I. M. Hall, BEDTools: A flexible suite of utilities for comparing genomic features. *Bioinformatics* **26**, 841–842 (2010).
130. Y. Liao, G. K. Smyth, W. Shi, featureCounts: An efficient general purpose program for assigning sequence reads to genomic features. *Bioinformatics* **30**, 923–930 (2014).
131. Z. Shao, Y. Zhang, G. C. Yuan, S. H. Orkin, D. J. Waxman, MAnorm: A robust model for quantitative comparison of ChIP-Seq data sets. *Genome Biol.* **13**, R16 (2012).
132. F. H. Mansour, D. G. Pestov, Separation of long RNA by agarose-formaldehyde gel electrophoresis. *Anal. Biochem.* **441**, 18–20 (2013).
133. G. M. Church, W. Gilbert, Genomic sequencing. *Proc. Natl. Acad. Sci. U.S.A.* **81**, 1991–1995 (1984).
134. G. S. Pall, A. J. Hamilton, Improved northern blot method for enhanced detection of small RNA. *Nat. Protoc.* **3**, 1077–1084 (2008).
135. H.-X. Deng, W. Chen, S.-T. Hong, K. M. Boycott, G. H. Gorrie, N. Siddique, Y. Yang, F. Fecto, Y. Shi, H. Zhai, H. Jiang, M. Hirano, E. Rampersaud, G. H. Jansen, S. Donkervoort, E. H. Bigio, B. R. Brooks, K. Ajroud, R. L. Sufit, J. L. Haines, E. Mugnaini, M. A. Pericak-Vance, T. Siddique, Mutations in UBQLN2 cause dominant X-linked juvenile and adult-onset ALS and ALS/dementia. *Nature* **477**, 211–215 (2011).
136. E. K. Schmidt, G. Clavarino, M. Ceppi, P. Pierre, SUnSET, a nonradioactive method to monitor protein synthesis. *Nat. Methods* **6**, 275–277 (2009).
137. K. Zhang, C. J. Donnelly, A. R. Haeusler, J. C. Grima, J. B. Machamer, P. Steinwald, E. L. Daley, S. J. Miller, K. M. Cunningham, S. Vidensky, S. Gupta, M. A. Thomas, I. Hong, S.-L. Chiu, R. L. Huganir, L. W. Ostrow, M. J. Matunis, J. Wang, R. Sattler, T. E. Lloyd, J. D. Rothstein, The *C9orf72* repeat expansion disrupts nucleocytoplasmic transport. *Nature* **525**, 56–61 (2015).
138. U. B. Pandey, Z. Nie, Y. Batlevi, B. A. McCray, G. P. Ritson, N. B. Nedelsky, S. L. Schwartz, N. A. DiProspero, M. A. Knight, O. Schuldiner, R. Padmanabhan, M. Hild, D. L. Berry, D. Garza, C. C. Hubbert, T. P. Yao, E. H. Baehrecke, J. P. Taylor, HDAC6 rescues neurodegeneration and provides an essential link between autophagy and the UPS. *Nature* **447**, 859–863 (2007).
139. I. Casci, K. Krishnamurthy, S. Kour, V. Tripathy, N. Ramesh, E. N. Anderson, L. Marrone, R. A. Grant, S. Oliver, L. Gochenaur, K. Patel, J. Sterneckert, A. M. Gleixner, C. J. Donnelly, M.-D. Ruepp, A. M. Sini, E. Zuccaro, M. Pennuto, P. Pasinelli, U. B. Pandey, Muscleblind acts as a modifier of FUS toxicity by modulating stress granule dynamics and SMN localization. *Nat. Commun.* **10**, 5583 (2019).
140. E. N. Anderson, L. Gochenaur, A. Singh, R. Grant, K. Patel, S. Watkins, J. Y. Wu, U. B. Pandey, Traumatic injury induces stress granule formation and enhances motor dysfunctions in ALS/FTD models. *Hum. Mol. Genet.* **27**, 1366–1381 (2018).
141. R. Core Team, *R: A Language and Environment for Statistical Computing* (R Foundation for Statistical Computing, 2022).
142. D. Bates, M. Mächler, B. Bolker, S. Walker, Fitting linear mixed-effects models using lme4. *J. Stat. Softw.* **67**, 1–48 (2015).
143. T. Hothorn, F. Bretz, P. Westfall, Simultaneous inference in general parametric models. *Biom. J.* **50**, 346–363 (2008).
144. A. K. Henras, C. Plisson-Chastang, M. F. O'Donohue, A. Chakraborty, P.-E. Gleizes, An overview of pre-ribosomal RNA processing in eukaryotes. *Wiley Interdiscip. Rev. RNA* **6**, 225–242 (2015).

Acknowledgments: J.K.I. is a New York Stem Cell Foundation—Robertson Investigator and the John Douglas French Alzheimer's Foundation Endowed Associate Professor of Stem Cell Biology and Regenerative Medicine. The content of this publication does not necessarily reflect the views or policies of the Department of Health and Human Services, nor does mention of trade names, commercial products, or organizations imply endorsement by the U.S. government. E.K. is a Les Turner ALS Center Investigator and a New York Stem Cell Foundation—Robertson Investigator. **Funding:** This work was supported by the U.S. National Institutes of Health (NIH) National Institute of Neurological Disorders and Stroke (NINDS) and National Institute of Aging (NIA) grant R01NS104219 (E.K.); NIH/NINDS grant R21NS107761 (E.K.); AFM-Telethon French Muscular Dystrophy Association Trampoline Grant #23648 (J.A.O.); AFM-Telethon postdoctoral fellowship (J.A.O.); Ramon y Cajal fellowships RYC2019-026980-I (J.A.O.) and RYC2021-033294-I (I.R.S.); Gipuzkoa Foru Aldundia 2019-FELL-000017-01 (I.R.S.); Maria de Maeztu Units of Excellence CEX2021-001159-M (J.A.O.) and MDM-2017-0720 (I.R.S.); NINDS grants R01NS097850 and R01NS131409 (J.K.I.); Department of Defense grants PR211919 and W81XWH2110131 (J.K.I.); John Douglas French Alzheimer's Foundation (J.K.I.); Center for Regenerative Nanomedicine at the Simpson Querrey Institute (S.I.S. and T.D.C.); Intramural Research Program, NIH, National Cancer Institute (NCI), Center for Cancer Research (M.B. and S. L.W.); Les Turner ALS Foundation (E.K.); and New York Stem Cell Foundation (J.K.I. and E.K.).
Author contributions: Conceptualization: J.A.O., I.R.S., M.B., A.C.F., S.L.W., and E.K. Methodology: J.A.O., I.R.S., M.B., A.C.F., T.R.F., Y.L., K.S., T.D.C., E.D.M., T.P.N., E.N.A., and J.A. Investigation: J.A.O., I.R.S., M.B., A.C.F., T.R.F., Y.L., K.S., T.D.C., E.D.M., T.P.N., E.N.A., and J.A. Visualization: J.A.O., I.R.S., M.B., and A.C.F. Supervision: J.K.I., U.B.P., S.L.W., S.I.S., and E.K. Writing—original draft: J.A.O., I.R.S., M.B., A.C.F., S.L.W., S.I.S., and E.K. Writing—review and editing: J.A.O., I.R.S., M.B., A.C.F., T.R.F., Y.L., K.S., T.D.C., E.D.M., T.P.N., E.N.A., J.A., J.K.I., U.B.P., S.L.W., S.I.S., and E.K. **Competing interests:** J.K.I. is a cofounder of AcuraStem Inc. and Modulo Bio; a scientific advisory board member of Spinogenix, Vesalius Therapeutics, and Synapticure; and a paid employee of BioMarin Pharmaceutical Inc. E.K. is a consultant for Confluence Therapeutics, Axion Biosystems, Synapticure, and ResQ Biotech. None of these companies were involved in this work. A provisional patent application (63/284,485) and a PCT application (PCT/US2022/051249) have been filed on this work. The authors declare no other competing interests. **Data and materials availability:** All data needed to evaluate the conclusions in the paper are

present in the paper and/or the Supplementary Materials. The accession number for the CLIP-Seq data reported in this paper is under GEO: GSE182008. All software used in this study is listed in Materials and Methods and publicly available. All iPSC lines and plasmids used in this study can be provided by the lead contact, E.K., pending scientific review and a completed material transfer agreement. Requests for these items should be submitted to: evangelos.kiskinis@northwestern.edu.

Submitted 13 November 2022
Accepted 11 October 2023
Published 10 November 2023
10.1126/sciadv.adf7997